

**CLOUD RADIATIVE FORCING AT THE TOP OF THE ATMOSPHERE DURING
FIRE ACE DERIVED FROM AVHRR DATA**

David R. Doelling
AS & M Inc.
Hampton, VA 23666

Patrick Minnis
Atmospheric Sciences
NASA-Langley Research Center
Hampton, VA 23681

Douglas A. Spangenberg, Venkatesan Chakrapani, Ashwin Mahesh
AS & M Inc.
Hampton, VA 23666

Shelly K. Pope, Francisco P. J. Valero
Center for Atmospheric Sciences
Scripps Institution of Oceanography
La Jolla, CA 92093

Journal of Geophysical Research
Volume 106, 15,279-15,296
July 27, 2001

Abstract

Cloud radiative forcing at the top of the atmosphere is derived from narrowband visible and infrared radiances from NOAA-12 and 14 Advanced Very High Resolution Radiometer (AVHRR) data taken over the Arctic Ocean during the First ISCCP Regional Experiment Arctic Cloud Experiment (FIRE ACE) during spring and summer of 1998. Shortwave and longwave fluxes at the top of the atmosphere (TOA) were computed using narrowband-to-broadband conversion formulae based on coincident Earth Radiation Budget Experiment (ERBE) broadband and AVHRR narrowband radiances. The NOAA-12/14 broadband data were validated using model calculations and coincident broadband flux radiometer data from the Surface Heat Budget of the Arctic Ocean experiment and from aircraft data. The AVHRR TOA albedos agreed with the surface- and aircraft-based albedos to within one standard deviation of ± 0.029 on an instantaneous basis. Mean differences ranged from -0.012 to 0.023 depending on the radiometer and platform. AVHRR-derived longwave fluxes differed from the model calculations using aircraft- and surface-based fluxes by -0.2 to -0.3 Wm^{-2} , on average, when the atmospheric profiles were adjusted to force agreement between the observed and calculated downwelling fluxes. The standard deviations of the differences were less than 2%. Mean total TOA albedo for the domain between 72°N and 80°N and between 150°W and 180°W changed from 0.695 in May to 0.509 during July, while the longwave flux increased from 217 to 228 Wm^{-2} . Net radiation increased from -89 to -2 Wm^{-2} for the same period. Net cloud forcing varied from -15 Wm^{-2} in May to -31 Wm^{-2} during July, while longwave cloud forcing was nearly constant at $\sim 8 \text{ Wm}^{-2}$. Shortwave cloud forcing dominated the cloud effect, ranging from -22 Wm^{-2} during May to -40 Wm^{-2} in July. The mean albedos and fluxes are consistent with previous measurements from the ERBE, except during May when the albedo and longwave flux were greater than the maximum ERBE values. The cloud forcing results, while similar to some earlier estimates are the most accurate values hitherto obtained for regions in the Arctic. When no significant melting was present, the clear-sky longwave flux showed a diurnal variation similar to that over land under clear skies. These data should be valuable for understanding the Arctic energy budget and for constraining models of atmosphere and ocean processes in the Arctic.

1. INTRODUCTION

Clouds have a significant impact on the Arctic radiation budget. During the winter months, they produce a net warming effect at the surface by decreasing the amount of longwave radiation lost to space. This trapping effect may be balanced during the summer by clouds reflecting solar radiation to space that would otherwise have warmed the surface. The change in the radiation balance due to clouds is termed radiative forcing. Estimates of cloud radiative forcing are sensitive to how well the cloudy and clear radiative fluxes are characterized, because the forcing depends on the radiative properties of both the clouds and the surface [Ramanathan *et al.* 1989]. A positive cloud radiative forcing (CRF) at the top of the atmosphere (TOA) indicates that the clouds cause a warming of the overall Earth-atmosphere system. Conversely, a negative value of CRF denotes a cooling of the system. The vertical distribution of the cooling or warming is not specified for this quantity. The response of the system may occur at the surface below the clouds or within the atmosphere above the clouds. Additional information is required to determine the response of the system to the forcing. CRF, however, is a fundamental quantity needed to constrain the effects of clouds within short or long-term climate models and should be determined as accurately as possible.

The similarities between clouds and snow-covered surfaces, at both solar and infrared wavelengths, as well as the large variability of the surface albedo, limits our ability to detect clouds using satellite data. As a result, cloud radiative forcing in the Arctic is an uncertain quantity; establishing its magnitude, sign, and seasonal variability is critical for assessing the role of clouds in the Arctic climate. The availability of a wide variety of surface, aircraft, and satellite measurements taken during the First ISCCP (International Satellite Cloud Climatology Project) Regional Experiment (FIRE) Arctic Clouds Experiment [ACE; Curry *et al.*, 2000] makes it possible to reduce the uncertainties in our estimates of cloud radiative effects in the Arctic.

The sensitivity of TOA CRF to uncertainties in the measurements and to changes in the cloud properties themselves is manifest in the large variability of current estimates for summertime values of this quantity. Data from the Earth Radiation Budget Experiment (ERBE) broadband scanner on National Ocean and Atmospheric Administration (NOAA) satellites, NOAA-9 & 10, were used to determine polar CRF between 1985 and 1989 [Harrison *et al.* 1990]. Winter CRF over the Arctic is positive because the clouds are generally colder than the surface and no shortwave CRF can occur. Harrison *et al.* [1990] found negative CRF over the Arctic during July 1985 using a relatively crude method to detect cloud amounts in the ERBE 50-km footprints. This forcing ranged from -100 Wm^{-2} at 75°N to -5 Wm^{-2} at 90°N . Curry and Ebert [1992] computed the TOA CRF over the Arctic using climatologies of surface-observed cloud amounts and average in-situ cloud microphysical properties adjusted to match ERBE fluxes. At 80°N , they also found negative CRFs of approximately -25 , -45 , and -70 Wm^{-2} during May, June, and July respectively. Rossow and Zhang [1995] estimated a much smaller negative forcing of roughly -30 Wm^{-2} during July at 80°N using ISCCP C2 cloud and surface properties in radiative transfer calculations. Schweiger and Key [1994] also computed CRF using ISCCP C2 products and found mean values of approximately -35 , -55 , and -60 Wm^{-2} during May, June, and July 1985-1989, respectively, for all ocean areas north of 62.5°N . Although new cloud retrievals are available from ISCCP [Rossow and Schiffer 1999], no CRF results have been published using the latest products. The newer ISCCP D2 datasets include additional cloud properties and show increased cloud amounts. Estimates of CRF using the D2 products are expected to differ from earlier values.

In this paper, a cloud amount dataset derived from the Advanced Very High Resolution Radiometer (AVHRR) data taken during FIRE ACE is used to provide a more accurate estimate of TOA CRF than heretofore possible. Because no broadband radiation data were taken by satellites over the Arctic during FIRE ACE, empirical narrowband conversion methods are used to estimate broadband fluxes from the NOAA-12 and NOAA-14 AVHRR radiances. The derived fluxes are verified by comparisons to theoretical calculations and to surface and aircraft radiation measurements. The results of these analyses provide a clearer picture of the role of clouds in the Arctic energy cycle, and can serve as the basis for improved modeling of Arctic cloud and energy processes.

2. DATA & METHODOLOGY

Unless indicated otherwise, LW and albedo quantities described in this paper refer to values at the top of the atmosphere.

2.1. Narrowband AVHRR data

Minnis et al. [2000] derived narrowband visible (VIS; 0.65 μm) albedo and infrared (IR; 10.8 μm) equivalent blackbody temperatures from intercalibrated NOAA-12 and NOAA-14 AVHRR High-Resolution Picture Transmission (HRPT) 1-km images collected during FIRE ACE between 3 May and 31 July 1998. The VIS albedo is

$$\alpha_v = L_v / [D(d) \mu_o E \chi(\theta_o, \theta, \psi)] \quad (1)$$

where D is the Earth-Sun distance correction factor for Julian day d , E is the visible solar constant for N14 (511 $\text{Wm}^{-2}\text{sr}^{-1}\mu\text{m}^{-1}$), and θ and θ_o are the satellite viewing and solar zenith angles, respectively. The VIS radiance is L_v , ψ is the relative azimuth angle, and $\mu_o = \cos\theta_o$. The narrowband bidirectional anisotropic reflectance factors χ from *Minnis and Harrison* [1984] were used for clear ocean and cloudy scenes, while the Earth Radiation Budget Experiment broadband bidirectional model [*Suttles et al.*, 1998] is used for clear snow or ice scenes. Each pixel was classified as clear snow, clear ocean, or cloud. *Minnis et al.* [2000] provide a complete description of the calibration, methodology, and accuracy of the results.

The pixel-level results for each of the 509 images were averaged on a 0.5° latitude by 2° longitude grid covering the area between 72° to 80°N and 180° to 150°W . This grid includes the varying position of the Surface Heat Budget of the Arctic Ocean (SHEBA) ship *Des Groseilliers* [*Perovich et al.*, 1999], initially centered near 76°N , 165°W . The cloud processing was only applied to images with $\theta \leq 45^\circ$ relative to the ship location; 70% of the images met this criterion. None of the images provides complete coverage of the domain for a given overpass, so there is incomplete sampling over the domain. The maximum number of samples for a given region (near the ship) ranges from 150 during July to 193 during June. As few as 7 samples were recorded for some regions in corners of the domain during a given month. The VIS albedo α_v , IR equivalent blackbody temperature T (hereafter referred to as simply IR temperature), and scene classification for each pixel were used to compute average values of cloud amount and the VIS albedos and IR temperatures for clear and cloudy conditions within each grid box [*Minnis et al.* 2000]. Also, for each image, the pixel-level values were averaged to obtain mean values of each quantity for circles of radius of 25 km centered on the *Des Groseilliers*.

A similar analysis was applied to NOAA-9 4-km AVHRR data taken during May, June, and July of 1986 over an area bounded by 65° and 75°N and 135° and 170°W . The NOAA-9

VIS reflectances were computed from the raw counts as in *Minnis et al.* [1993]. The VIS albedo, IR temperature, and cloud fraction were computed for each 2.5° latitude-longitude box in the 1986 domain following the methods of *Minnis et al.* [2000].

The IR temperatures were converted to IR fluxes using the approach of *Minnis et al.* [1991]. The narrowband flux is

$$M_{ir} = 6.18 L_{ir}(0^\circ), \quad (2)$$

where the IR radiance at a viewing zenith angle of 0° is

$$L_{ir}(0^\circ) = B(T) / \gamma(\theta), \quad (3)$$

where $B(T)$ is the Planck function computed at a wavelength $\lambda = 10.8 \mu\text{m}$ and γ is the limb-darkening function from *Minnis and Harrison* [1984]. The limb-darkening function produces a change in radiance of less than 5% for $\theta < 70^\circ$. It may not be representative of many of the observed scenes because it was derived for an average of 45 different atmospheric profiles. However, it is primarily used to provide a consistent normalization for estimating broadband flux from the IR data.

2.2. ERBE data

The May-July 1986 2.5° latitude-longitude NOAA-9 ERBE [*Barkstrom et al.* 1989] shortwave (SW; 0.2 – 5.0 μm) albedos α_{sw} and longwave (LW; 5.0 – 50 μm) fluxes M_{lw}' were screened to eliminate viewing zenith angles greater than 45° and solar zenith angles exceeding 84° for the 1986 domain. These fluxes are coincident with the NOAA-9 AVHRR data. Due to calibration problems in the NOAA-9 ERBE LW fluxes, the values of the original fluxes M_{lw}' were corrected using the method of *Thomas et al.* [1995] to account for an earlier underestimation of LW flux. The values of LW flux used in this study are

$$M_{lw} = M_{lw}' + 0.021 M_{sw}, \quad (4)$$

where M_{sw} is the shortwave flux and the coefficient of 0.021 is based on the mean correction factor slope of -0.036 divided by 1.71, the average value of the SW spectral correction factor for polar clouds [*Green and Avis* 1996]. It is assumed that most of the scenes in this domain were identified by ERBE as overcast or mostly cloudy because few clear-sky flux values were available. This correction resulted in an average increase of $\sim 7 \text{ Wm}^{-2}$ in the LW flux compared to the original AVHRR ERBE values. Due to the small differences between the clear and cloudy albedos, however, the effect of this correction on the LW cloud radiative forcing should be minimal. Some disagreement remains concerning the origin of this LW error. *Thomas et al.* [1995] ascribe it to an error in the ERBE SW channel. *R. N. Green* (personal communication, 1999) has concluded that the error is in the SW part of the ERBE total channel. As this uncertainty is not yet resolved, no corrections are applied to the SW fluxes.

2.3. Other data

2.3.1 Atmospheric profiles

Temperature and humidity profiles taken near 0000, 0600, 1200, and 1800 UTC with rawinsondes launched from the *Des Groseilliers* were used to characterize the vertical

atmospheric structure for the domain during FIRE ACE. These soundings were interpolated to the time of each overpass and are assumed to be representative of the entire domain. The National Center for Environmental Prediction (NCEP) 12-hourly gridded temperature and humidity analyses for 1986 were used for developing the infrared-to-longwave flux formula. These values were interpolated to the time of the NOAA-9 overpasses.

2.3.2 Radiometer data

Broadband flux data were available from the National Center for Atmospheric Research C-130Q aircraft and the SHEBA ice camp [Curry *et al.* 2000]. The ice camp radiometers were on the SHEBA Atmospheric Surface Flux Group 20-m-high tower at the main SHEBA camp and consisted of up- and downwelling precision infrared radiometers and shortwave spectral pyranometers with a normal incidence pyrliometer for direct beam broadband shortwave radiance [Andreas *et al.* 1999]. The data were made available as hourly averaged fluxes. The C-130Q was equipped with up- and downlooking NCAR-modified Eppley PSP pyranometers (0.285 – 2.80 μm) and NCAR-modified Eppley PIR pyrgeometers (3.5 to 50 μm). As of this writing, details on the NCAR Eppleys and their attitude corrections can be found online at the following Uniform Resource Locator (URL) http://www.atd.ucar.edu/dir_off/airborne and in Bannehr and Glover [1991]. It also included up- and downlooking Radiation Measurement System (RAMS) total shortwave broadband radiometers (TSBR; 0.224- 3.91 μm) and the infrared broadband radiometer (IRBR; 3.5 – 35 μm). Details of the RAMS instruments can be found in Valero *et al.* [1997]. All of the data were adjusted to account for variations in aircraft attitude. The airborne radiometer data are available at sampling rates of less than 1 Hz.

2.3.3 Calculations of TOA fluxes and albedos from surface and aircraft radiometer data

2.3.3.1 General approach to modeling

All comparisons between satellite and radiometer data were performed at the TOA. The radiative transfer model of Fu and Liou [1993], hereafter referred to as FL, as implemented by Charlock and Alberta [1996] was used to translate the surface and aircraft measurements to the TOA. For surface data, the TOA SW albedos and LW fluxes were also computed using the model *Streamer* [Key and Schweiger 1998] to help estimate the uncertainties in the model calculations and input. Downwelling LW flux was also computed with the FL model to determine the consistency of the model results relative to the radiometer measurements. For comparisons between the surface and AVHRR data using the FL model, temperature and humidity profiles were specified for the layer between the surface and 100 hPa using the nearest sounding, while the NCEP profiles of Gupta *et al.* [1995] provided temperatures and humidities for the upper atmosphere and the ozone concentrations for the entire atmosphere. For the *Streamer* calculations, the SHEBA soundings and NCEP analysis profiles were used to specify the temperature and humidity up to 100 hPa and above 100 hPa, respectively. Ozone concentrations for the entire atmosphere were taken from the NCEP profiles. For the aircraft-satellite comparisons, the soundings from either the SHEBA camp or Barrow, Alaska, depending on which was closer, were used to specify a vertical profile of temperature and humidity up to 100 hPa. Although the aircraft were sometimes hundreds of kilometers away from these sites, they were nevertheless the closest weather stations from which routine soundings were available. Temperatures and humidities for the upper atmosphere and the ozone concentrations for the entire atmosphere were specified using the profiles of Gupta *et al.* [1995]. For all FL calculations, an average continental aerosol with an optical depth of 0.085 [d'Almieda *et al.*

1991; Hess *et al.* 1998] was specified and distributed vertically according to the profiles of *Spinhirne* [1991]. The optical depth value used here is from a May-July climatological mean [B. Soden, personal communication] estimated with the same procedure used by Haywood *et al.* [1999]. An Arctic haze aerosol with an optical depth of 0.1 was specified for the Streamer calculations.

To compute the TOA albedo, the models require a specification of the broadband albedo at the bottom of the atmosphere. The albedos measured at the tower are used for the surface-AVHRR comparison, while the albedos measured at the aircraft are used for the C-130-AVHRR comparisons. Everything below the aircraft is treated as if it were a surface, so that only the atmosphere above the aircraft affects the calculations. The FL model partitions the specified albedo into 6 SW spectral bands with weightings corresponding to the relative distribution of the spectral albedo for the particular underlying surface. In this study, the normalized spectral shapes of ocean albedo from Bowker *et al.* [1985] and the Antarctic snow albedo of Grenfell *et al.* [1994] were used to determine the partitioning of the measured albedos at the surface and at aircraft level. The choice of a particular shape depended on the scene classification. Underlying clouds were specified as liquid water clouds with optical depths between 1 and 5. The spectral variation of the surface was included for snow, ocean, and tundra depending on the location of the aircraft.

The LW flux at the TOA was computed using the atmospheric profiles with a specification of the upwelling flux at the bottom of the atmosphere. For the surface-AVHRR comparisons, the upwelling flux at the bottom was specified by varying the skin temperature in the FL model until the flux computed at the tower level matched the corresponding value of M_{LWS} . For the *Streamer* calculations, the mean clear-sky radiative temperature from the satellite was used to specify the surface skin temperature for the LW calculations. It was assumed that atmospheric attenuation of the 10.8- μm radiances was insignificant in the clear Arctic skies and that the surface emissivity at 10.8 μm represented that of the entire LW spectrum. The upwelling LW flux measured by the aircraft radiometers was used to specify the flux at the bottom of the atmosphere in the models. This was accomplished by adjusting the surface skin temperature until the calculated flux at flight altitude matched the observed upwelling value.

2.3.3.2 Surface-based comparisons

Only clear-sky surface radiometer data were compared with the satellite results. To be considered clear, the AVHRR scene classification for the ship circle was required to be entirely clear and the cloud observations taken visually at the ship [see Minnis *et al.* 2000] before and after the satellite overpass were also required to be clear. Thus, the observations that met this criterion were typically taken during a 6-hour long period of clear skies. Only 13 separate satellite overpasses met these stringent criteria for comparison with the surface datasets. Because of the low-resolution of the surface radiometric datasets, the values of surface albedo and M_{LWS} used in the models were linearly interpolated between the hourly means to obtain a value corresponding to the AVHRR overpass time. Similarly, the downwelling longwave flux M_{LWSd} was also linearly interpolated to the time of the AVHRR measurement time.

2.3.3.3 Aircraft comparisons

The aircraft data were used when they were coincident with AVHRR overpasses and the C-130Q was in straight-line flight at a constant altitude. The highest altitude segments were selected to minimize the correction of the fluxes at aircraft level to the TOA; these altitudes

ranged from 2.5 to 6.2 km. Data were used only if flight logs indicated clear skies above the aircraft and there was minimal variability in the aircraft attitude and in the observed downwelling fluxes. Both May and July flights were used in the albedo comparisons, while only July Eppley PIR data were used for the LW comparisons because of technical problems with the PIRs during May. To compare with the AVHRR results, mean fluxes were computed for flight segments centered on the AVHRR overpass time with a window of up to 30 min. Continuous segments were split into two or more legs if sudden changes in albedo occurred due to passage over a different scene type. These scene type changes were confirmed by examination of the AVHRR imagery. A total of 16 legs were obtained from 10 different continuous segments. The satellite scene classification was used to select a model for use in (1). The corresponding AVHRR pixel fluxes and albedos were averaged over a one-pixel-wide line coincident with the C-130Q flight leg to match the aircraft fluxes. One third of the data was taken over clear snow (one clear ocean case), one third was taken over thin clouds over snow, and the remaining third was taken over thick clouds over snow or tundra.

The TOA albedo was determined by matching the aircraft-measured albedo with the model-computed albedos at the flight altitude as discussed above. Then the matching profile was followed to the TOA to obtain an estimate of α_{sw} . An example set of profiles is shown in Figure 1 for May 4 for two solar zenith angles (SZA) as noted by μ_o ; the flight level is 6 km. If the aircraft-measured albedo is 0.57 at $\mu_o = 0.3$, then the solid curve would be followed to obtain an albedo of ~ 0.53 at the TOA.

The LW TOA fluxes were estimated following a similar procedure except that the atmospheric profile was first adjusted prior to making the calculations. It was assumed that the calculated downwelling flux must match the observed downwelling radiation at the aircraft. This requirement was employed because the LW flux is more sensitive to atmospheric variations of temperature and humidity in the upper troposphere than the SW flux. Because the SHEBA sounding may not be representative of the vertical atmospheric profile at the aircraft location, the modeled downwelling flux was adjusted to match the aircraft value by altering the vertical profile of humidity above the aircraft. This was accomplished by increasing the relative humidity by up to 100% in 10% increments for all layers from 200 hPa to flight altitude and in 5% increments for all layers between 100 and 200 hPa. The resulting profiles are not necessarily the correct values of temperature and humidity, but they ensure that the model calculations are consistent with the aircraft data in at least one direction. Although many different corrections could have been used, the humidity corrections were applied here because of their simplicity and because the humidity is probably more uncertain. The altered atmosphere and surface temperature were then used to compute the TOA LW flux. No attempt was made to alter the atmospheric profile to match the satellite observed fluxes. Thus, the results are independent of and can be compared to the satellite fluxes.

2.4. Conversion to broadband albedos and fluxes

Narrowband radiances can be used to determine accurate mean broadband fluxes averaged over a period of time when the narrowband data are tuned to the particular instruments and region [Minnis *et al.*, 1991; Doelling *et al.* 1998; Valero *et al.* 1999]. So far, no conversion algorithms have been specifically developed for the Arctic region. To obtain the broadband CRF, the broadband fluxes are computed from the AVHRR data using the regression formulae developed below using the approach of Minnis and Smith [1998].

The matched 1986 NOAA-9 ERBE and AVHRR albedos are shown in Figure 2 with examples of several lines for constant SZA resulting from the regression equation:

$$\alpha_{sw} = 0.0293 + 0.721 \alpha_v + 0.0301 \alpha_v^2 + 0.0869 \ln(1/\mu_o). \quad (5)$$

The squared correlation coefficient is 0.966 and the rms difference between the ERBE and AVHRR-predicted albedos is 0.0343 representing a relative error of 6.5%. The regression used 670 data points. The observed values generally correspond to the increase in SW albedo with SZA for a given value of VIS albedo. This tendency was also reported by *Minnis and Smith* [1998] for a similar regression analysis from data taken over a land surface.

Figure 3 shows the scatterplot and regression results for the matched IR and LW fluxes. The lines are from constant values of relative humidity RH above the altitude corresponding to the observed value of T . The LW flux is

$$M_{lw} = 65.7 + 7.64 M_{ir} - 0.055 M_{ir}^2 - 0.247 M_{ir} \ln(RH). \quad (6)$$

Values of RH for determining the regression fits were computed from the NCEP data as the column-weighted relative humidity (in percent) above the radiating surface. For consistency, RH was estimated during the FIRE ACE period from the SHEBA soundings using only the standard levels in the NCEP product. For the 615 data points, the squared correlation coefficient is 0.88 and the rms difference is 5.7 Wm^{-2} , a relative uncertainty of 2.5%. The data points corresponding to a given range of RH are generally consistent with the regression result which shows an increase of LW flux for a given IR flux as RH decreases. The regression fits in Figures 2 and 3 are not necessarily valid for other domains and seasons because a different set of surface conditions and atmospheric profiles may produce different relationships between the narrowband and broadband fluxes at the TOA [e.g., *Minnis and Smith* 1996, *Minnis et al.* 1991].

Equations (5) and (6) were applied separately to the gridded clear and cloudy AVHRR narrowband data taken during FIRE ACE to obtain SW and LW fluxes for all cloudy and clear pixels separately. Figure 4 shows an example of the results for an N12 image taken at 1936 UTC, 19 May 1998. Several extensive low cloud decks cover most of the scene with a large bright cloud-free strip along the center of the image. Despite the relatively thick cloud cover, the leads are visible through the clouds in the VIS image. Most of the clouds have a lower reflectance than the adjacent clear areas. After correcting for bidirectional reflectance differences, however, the VIS (not shown) and SW albedos of the clear areas are slightly less than the nearby cloudy areas. Cloud edges on the eastern and southern sides of the oval-shaped cloud deck in the lower left corner are brighter than the interior. The northern and western edges are much darker than the deck's interior. Clear areas adjacent to the northern and western edges are in shadow and are the darkest parts of the scene. Although warmer than the lower clouds to the east and north, this oval cloud mass apparently is much thicker because it shows the edge effects. The extreme effects due to the cloud geometry are not taken into account with the anisotropic bidirectional reflectance models.

2.5. Cloud forcing

The standard definitions of LW, SW, and net CRF are, respectively,

$$\text{LWCRF} = M_{lw \text{ CLR}} - M_{lw}; \quad (7)$$

$$\text{SWCRF} = S[\alpha_{\text{SWCLR}} - \alpha_{\text{SW}}]; \quad (8)$$

and

$$\text{NETCRF} = \text{LWCRF} + \text{SWCRF}, \quad (9)$$

where S is the incoming solar flux for the particular solar zenith angle and Earth-sun distance and subscript CLR refers to the clear-sky condition. The instantaneous measured fluxes were interpolated to every local hour using ERBE time-space averaging techniques [Young *et al.* 1998] to minimize the effects of the AVHRR sampling patterns. The resulting fluxes were used to compute hourly CF parameters as well as the net flux,

$$M_{\text{net}} = S(1 - \alpha_{\text{SW}}) - M_{\text{lw}}. \quad (10)$$

All of the parameters were then averaged over all hours to determine monthly means and monthly hourly means. The albedos were averaged using μ_o -weighting To account for the variation of incoming solar radiation with μ_o . Mean clear-sky albedo, LW flux, and net flux were computed using only the clear portion of each grid box during a given overpass when the cloud amount in the grid box was less than 90%. This screening criterion was used to minimize shadow or three-dimensional cloud effects resulting from the high solar zenith angles. Results are reported here only for those regions that had more than 55, 72, and 54 samples during May, June, and July, respectively, to avoid spurious anomalies that may occur because of biased sampling times. The results include more than 79% of the regions within the domain.

3. RESULTS

Figure 5 shows the mean clear-sky and total albedos for each of the months. During May, the clear-sky albedos range from 0.61 in the south to 0.70 at the northern edge of the domain. All of the albedos drop dramatically during June resulting in a south-to-north variation between 0.46 and 0.59. Ponds began to appear on the ice near the SHEBA camp around the beginning of June. The diminished clear-sky albedos during June are consistent with ponding and a breakup of the ice pack in the south. By the end of July, the clear-sky albedos dropped another 0.1 resulting in a range from 0.35 along the southern edges to 0.50 in the north. Significant areas of nearly ice-free water occurred along the southern boundary of the domain. The addition of clouds yields total albedos that are greater in all cases, varying from 0.66 to 0.72 during May down to a range of 0.42 to 0.60 during July.

The clear LW fluxes are characterized by a 14 Wm^{-2} north-south gradient during May that is replaced by a less variable flux during June as the surface heats up (Figure 6). During July, the surface is warmer still, with only a 5 Wm^{-2} north-south gradient. The total LW flux reflects the presence of colder clouds because it drops at all locations. The gradient in M_{lw} is generally north-to-south, except during June when the cloud gradient is from east-to-west [Minnis *et al.* 2000]. During July, the SHEBA camp is located in an area with the maximum cloud cover and, correspondingly, is near the minimum in M_{lw} .

Differences in the clear and total albedos and fluxes are more easily seen in the CRF distributions in Figure 7. SWCRF varies from -10 to -35 Wm^{-2} during May. As the surface albedo decreases, the SW cloud forcing increases during June and July to values between -25 and

-65 Wm^{-2} . The greatest SWCRF occurs during July near the ship. The changes in LWCRF are less dramatic. North of the ship during May, LWCRF barely rises above zero reflecting the dominance of low clouds in that area. LWCRF varies from 3 to 16 Wm^{-2} during May and July. The gradients reverse from May to July with low relatively warm clouds dominating in southern part of the domain during the latter period. The net forcing is negative during all 3 months indicating that the clouds temper the warming of the Arctic during the summertime. Because the SW forcing is considerably larger in magnitude than the LW forcing, the distributions of NETCRF are similar to the SWCRF patterns. As a result of cloud cover, the radiative energy in the northern part of the domain is reduced by up to 50 Wm^{-2} during July. In May, the overall cloud effect is much smaller, ranging from -5 to -27 Wm^{-2} .

Table 1 summarizes the AVHRR-based monthly mean radiation results for the entire domain. The total albedos are greater than the clear albedos in the FIRE ACE domain by an average of 0.053 to 0.086. Accounting for the mean cloud amounts --70.1, 73.6, and 69.4% respectively during May, June, and July [Minnis *et al.* 2000] -- and the difference between the total and clear albedos, it was determined that the cloudy sky albedos are 0.718, 0.616, and 0.547, during May, June, and July, respectively; these values are 0.076 to 0.123 greater than the clear albedos. The albedo differences translate to SWCRF differences of -22 to -39.5 Wm^{-2} . The mean LW fluxes increase for both total and clear conditions as the season progresses with the cloudy-sky LW fluxes ranging from 214.1 Wm^{-2} in May to 224.5 Wm^{-2} in July. The overall LWCRF remains low during the entire period between 7 and 9 Wm^{-2} . The net flux is strongly negative during May but is almost nil by the end of July for the total sky case. With the onset of melting during June, the clear-sky net radiation increases by almost 80 Wm^{-2} from May through June, becoming significantly positive by July. This increase in absorbed solar energy produces only a $10\text{-}12 \text{ Wm}^{-2}$ increase in clear LW flux suggesting, in the absence of any net advective effects, that much of the absorbed solar energy was used in heating ice until it reached the melting point, melting ice, and evaporating water during June and July. During May, the absorbed SW flux primarily heated the ice. The surface air temperatures at the ship reflect this change in the energy distribution. The mean air temperature rose from -9.0°C to -0.7°C from May to June and by an additional 0.7°C from June to July. The clouds reduced the net warming of the system by 15 to 31 Wm^{-2} producing a negative mean net flux for all conditions throughout the FIRE ACE period considered here.

Diurnal variations of these parameters were also computed using the hourly means. Figure 8 shows the albedos as a function of local time for each month with the mean hourly values of μ_o . The clear-sky albedos are relatively flat with variations of less than 0.03 over a given day. Total sky albedo is more variable with minima occurring shortly after local noon and with maxima near local midnight when μ_o ranges from 0.09 to 0.16 during the period. The total albedo variation shows the impact of the clouds which generally become more reflective with decreasing μ_o . The LW fluxes in Figure 9 have less variability with a maximum mean diurnal range that is less than 4 Wm^{-2} during all months. Some of the diurnal variability is due to the clear-sky LW fluxes increasing to a maximum shortly before local noon. However, the diurnal range in total flux equals or exceeds that in the clear-sky flux during all 3 months suggesting a consistent diurnal variation in the clouds. Minnis *et al.* [2000] found that the cloud cover peaked shortly before noon during all 3 months. Several scenarios could account for the peak in LW flux coinciding with maximum cloud amount and the greater range in total LW flux compared to its clear counterpart. The mean cloud cover occurring during the late morning to mid-afternoon may have frequently been warmer than the surface, especially during May and June. Minnis *et al.*

[2000] found that the frequency of elevated temperature inversions decreased from 90% to 30% from May to July. The diurnally dependent occurrence of clouds in such inversion layers could help explain the diurnal variations seen in Figure 9. Additionally, the clouds may have been thin enough so that surface warming occurred and was detectable through the clouds or the clouds may have been slightly colder during the early morning. Further, the difference between the clear and total LW flux diurnal cycles may be an artifact of the data processing. The averaging process assumed that the ice acted like the ocean in that its skin temperature was assumed to vary linearly with time. The relatively high-resolution temporal sampling of the domain over the course of a day, however, should minimize the effects of that assumption.

Figure 10 shows the diurnal variation of CRF for the domain. The cloud impact is strongest when SWCRF (Figure 10a) reaches its minimum values around 0700 and 1900 LT as a consequence of the cloud diurnal variability, the solar zenith angle, and the cloud albedos. Even as the cloud cover and μ_o increase toward local noon in the morning, the decreasing cloud albedo reduces the amount of reflected SW radiation. The maximum cloud amount is reflected in the inflection of the curves near 1100 LT during each month. The absolute minimums occur during early afternoon and around midnight. In the latter case, the sun angle primarily responsible, while the reduced cloud amount determines the mid-afternoon absolute minimum. LWCRF (Figure 10b) is extremely flat, except during June. Thus, the diurnal variability in M_{lw} (Figure 9) during May and July was due to the lack of a variation in mean cloud temperature. The 1 Wm^{-2} dip in LWCRF during June suggests either a slight decrease in the coverage by high clouds or that the clouds forming before noon were warmer than the surface. Net cloud forcing (Figure 10c) mimics SWCRF because LWCRF lacked any substantial diurnal variability. Throughout the entire day for all 3 months NETCRF is negative, a phenomenon that is probably unique to the polar regions.

4. DISCUSSION

4.1. Error sources

The determination of radiative fluxes from satellite narrowband radiances is affected by many sources of uncertainty. The calibration of the narrowband instruments used to develop and apply the broadband conversion formulae must be consistent to eliminate bias. Coincident data from NOAA-9 and either NOAA-12/14 are necessary to directly determine the consistency in the calibrations. Although there was an overlap period between NOAA-9 and NOAA-12 during the early 1990's, comparison of data from that time period would be meaningless for data taken during the late 1990's. NOAA-12 and 14 are intercalibrated to within $\pm 3.2\%$ [Minnis *et al.* 2000], while the NOAA-14 VIS calibration is accurate in an absolute sense to $\pm 5\%$ [Rao and Chen 1996?]. The bidirectional reflectance or limb-darkening models used to convert the radiances to flux are the single greatest source of error in because of the highly variable nature of the radiance anisotropy. These errors are incurred in the conversion of broadband radiances to flux by ERBE and in the conversion of the narrowband radiances to fluxes or albedos in (1) – (3). The instantaneous error in the broadband albedo and the longwave flux due to uncertainty in the bidirectional reflectance or limb-darkening correction has been estimated at 12.5% and 5.2%, respectively [Wielicki *et al.* 1995]. Misclassification of the scene can affect the selection of the anisotropic correction models and the average clear or cloudy flux. If either value is biased, the net cloud radiative forcing will also be biased. The conversion of narrowband data to broadband fluxes also has uncertainties that can significantly affect the instantaneous values, while being smaller for monthly averages. Assessing each of these uncertainties individually and

combining them to obtain a single error for each flux is a difficult task. However, at a minimum the albedo and longwave flux are expected to agree to no more than the uncertainties in the anisotropic corrections on an instantaneous basis. The agreement should be much better when averaged over many samples. Comparisons with other estimates or measurements of the radiation fields provide an alternative, independent approach to assessing the quality of the derived fluxes.

4.2. Comparisons with surface data

The SW albedos derived from the AVHRR data are compared in Figure 11 with albedos computed with the FL and *Streamer* models using coincident surface albedos in clear skies. The satellite-derived albedos are generally higher than the FL values for the brightest scenes, while the surface data yield greater values for the middle range of albedos. *Streamer* gives slightly better agreement over the entire range of albedo. For these 13 data points, the mean differences between the satellite and model-calculated clear-sky albedos are -0.001 and -0.012 for the FL and *Streamer*, respectively. The corresponding standard deviations are 0.035 and 0.023. The mean standard deviation of the pixel albedos within the circle centered on the ship is ~5% of the AVHRR albedo.

The model-based estimates of the TOA albedo are remarkably close to the satellite results given all of the possible sources of error in the measurements and the model calculations. Downwelling diffuse SW radiation is typically underestimated by pyranometers due to radiative cooling of the instrument [e.g., Kato *et al.* 1997]. Thus, the surface albedo may be overestimated, resulting in a subsequent overestimation of the TOA albedo. The FL-calculated downwelling SW flux exceeds the Eppley-observed value by 8%. Some of this discrepancy may be due to differences in the spectral range, but it is likely that the diffuse radiation problem affects the observations. The true anisotropy in the reflectance field may differ from the corrections used in the satellite estimates. Each of the AVHRR albedos is within less than 9% of the FL results indicating that all of them are well within the expected anisotropic correction uncertainty. Because the satellite views the area from different angles during each overpass, this type of uncertainty should be a random-like effect and may tend to average out over several overpasses as seen in the average differences. Similarly, there are also some random errors associated with the narrowband-to-broadband albedo conversion and with the variation within the satellite pixels used to compute the means for each comparison. The standard error of the regression-fit in Figure 2 (0.034) is nearly identical to the standard deviations in the model-observation comparisons in Figure 11. Thus, the level of random uncertainty is equivalent to the uncertainty in the narrowband-broadband regression.

It is assumed that the SHEBA surface albedo represents the area viewed by the satellite. This assumption may not be valid because the albedo varies considerably on the small scale, especially when melting occurs. The 1-km scale variability within the radius of comparison can account for about half of the differences between the surface and satellite observations at the one standard deviation level. However, this variability is probably not representative of the small-scale albedo variations.

A random error would result from the differences between the actual and assumed aerosol properties in the calculations. If they were systematically under- or overestimated, a bias in TOA albedo would occur. To test the sensitivity of the calculations to aerosol type, an aerosol composed of 12% black carbon, a percentage that exceeds that for the continental aerosol, and 88% dust was inserted in the model with an optical depth of 0.085. It reduced the computed

TOA albedo by $\sim 2\%$ which would result in the satellite albedos exceeding the surface-based FL calculations by 0.012. A clean maritime aerosol has minimal absorption. It raises the FL TOA albedo by 0.01 relative to the continental aerosol results. A variation of ± 0.05 in the continental aerosol optical depth changes the TOA albedo by approximately $\pm 1\%$ depending on the surface albedo. Thus, the aerosol loading is an important factor in determining the mean difference. Assuming that the aerosol used here is representative of the mean aerosol conditions, it can be concluded that the mean AVHRR albedo is within the expected range of albedos. Another potential source of bias is error in the pyranometer calibrations. A calibration comparison of all of the surface radiometers is planned by the SHEBA Science Team.

Given all these error sources, the results plotted in Figure 11 are quite reasonable. The random errors are no larger than expected and the mean differences are consistent with an underestimate of the diffuse radiation at the surface or with inadequate specification of the aerosol loading. Coincident measurements of aerosol optical depth and type would greatly enhance these comparisons. Additional analysis of selected aircraft data are needed to determine how well the SHEBA-based albedos represent those within the AVHRR circle of comparison and a complete evaluation of the radiometer calibrations is needed to determine the expected errors in the pyranometer data.

The clear-sky TOA LW fluxes computed with the models are well correlated with the satellite-derived values (Figure 12). The *Streamer*-computed TOA LW fluxes are $2.5 \pm 3.5 \text{ Wm}^{-2}$ (one standard deviation, σ) greater than the AVHRR results, while the FL fluxes are $4.2 \pm 2.1 \text{ Wm}^{-2}$ greater than the satellite data. The average standard deviation of the AVHRR LW flux in the circle for a given overpass is 2.7 Wm^{-2} . The clear-sky downwelling LW fluxes (DLF) at the surface computed by the FL model are compared to the measured downwelling fluxes in Figure 13. The FL values average 8.9 Wm^{-2} less than the Eppler values, similar to the differences between the Eppler values and the *Streamer* results computed for the same conditions. Since the up- and downwelling differences suggest that both models produce insignificantly different results, only the FL model is used for the remainder of this study.

The complementary differences between the calculated and observed fluxes at the TOA and the surface suggest that the atmosphere may be moister than indicated by the radiosondes or that both models tend to underestimate the flux. Normalizing the model results to the surface measurements can account for any errors in the moisture profile or to errors in the model, but not for the surface radiometer measurements. The humidity at each level was incrementally increased or decreased to bring each of the FL results into agreement with the observed downwelling LW flux (DLF). The procedure used was identical to that described in section 2.3.3.3. Using the resulting humidity profile to compute the TOA fluxes reduces the mean TOA LW flux difference between the FL and AVHRR data to $-0.3 \pm 2.4 \text{ Wm}^{-2}$. The individual results are plotted in Figure 12. The average 3.7 Wm^{-2} decrease in M_{lw} for a 8.9 Wm^{-2} increase in DLF indicates that the atmosphere accounts for about 40% of the TOA LW flux for clear summertime Arctic conditions. This exercise also suggests that the mean differences between the AVHRR and model-computed LW fluxes in Figure 12 may be due to errors in the model or in the soundings. The soundings were interpolated to match the satellite overpass, but it is unlikely that they would have to be adjusted in the same direction for atmospheric humidity in all cases. Thus, errors in the models or the surface radiometers are likely sources of bias errors in the calculations. Thus, the mean differences between the model-computed and AVHRR TOA LW fluxes can be explained by the uncertainties in the model and in the radiometer calibrations.

4.3. Comparisons with aircraft data

Figure 14 shows the comparison of the AVHRR albedos with the May and July C-130 Eppley and RAMS flux measurements adjusted to the TOA. The AVHRR albedos are generally greater than their Eppley counterparts with less scatter than seen in Figure 11. The mean difference between the AVHRR and Eppley albedos is 0.021 ± 0.037 . Conversely, the RAMS albedos are typically a bit larger than the AVHRR values with no scene dependence. The mean difference is -0.006 ± 0.029 . This latter random error is smaller than the regression error in the AVHRR-based broadband albedos (see Figure 2).

The albedos are subject to the same type of errors discussed for the surface comparisons. However, uncertainties in the model atmosphere have much less impact because most of the moisture and aerosols are in the atmosphere below the aircraft. Use of several different Arctic atmospheres introduced errors no greater than 0.003 in the derived TOA albedos. The variety of scenes should also reduce the anisotropic correction error for the satellite data. Much of the error should depend on calibration of the radiometers. The Eppley radiometers are nominally accurate to within $\sim 10 \text{ Wm}^{-2}$ which translates to an albedo error of 0.016 for the dataset in Figure 14. However, they still require calibration maintenance when used on the aircraft. It is not clear how the Eppley calibrations were performed. The RAMS instruments were calibrated before and after each of the two periods when the C-130Q flew (May and July). The mean RAMS and AVHRR difference is less than the standard error of the mean, which is 0.007 for these 16 datapoints. Also, this mean difference falls between the TOA albedo differences with AVHRR found for the surface and C-130 Eppley results. Relative to the model-adjusted surface and aircraft radiometer data, the mean albedos derived with the NOAA-12 and 14 AVHRR data are accurate to within 0.001 ± 0.009 and the instantaneous results have a $1-\sigma$ uncertainty of 7%. These results also confirm that the 1986 albedo correlations in Figure 2 are applicable to the FIRE ACE period and may be accurate for other summertime periods within the domain.

Figure 15 plots the TOA-adjusted LW fluxes from the July Eppley data with the coincident AVHRR values. The two quantities are well correlated with a squared linear correlation coefficient of 0.78 and a mean difference of -0.2 Wm^{-2} with a standard deviation of 2.6 Wm^{-2} or 1.1%. Although this plot contains only 10 data points, the small variance suggests that the mean difference is accurate to within 1 Wm^{-2} if a normal distribution of differences is assumed. The standard deviation is less than that found for the original regression between ERBE and AVHRR. The agreement is much like that found for the 13 clear-sky cases over the SHEBA when the model calculations were forced to agree with the surface data by altering the soundings. While artificial changes in the soundings may introduce additional errors, they provide a means to ensure that the model produces values comparable to those measured by the aircraft (surface) instruments. Thus, nominally the difference between the satellite and modeled LW fluxes should be due to calibration errors and the anisotropic corrections for the AVHRR data. In this case, the agreement is remarkable and, together with the surface-based comparisons, it provides a high degree of confidence in the AVHRR-derived LW fluxes for the FIRE ACE period.

The comparisons between the surface and aircraft data with the AVHRR data are summarized in Table 2. The mean differences and standard deviations between the surface-based and AVHRR TOA albedos were averaged to obtain a single mean and standard deviation. Likewise, the average albedo difference and standard deviation are computed for the two aircraft datasets. These two mean differences and standard deviations were used to compute an overall mean difference and standard deviation by weighting each value by the number of samples. The

results, shown in the last row of Table 2, indicate the mean TOA albedo computed with 29 samples or more should be accurate to 0.001 ± 0.005 (the uncertainty bounds are the standard error in the mean for 29 samples) relative to the best estimate of TOA albedo derived from the coincident aircraft and surface data. The instantaneous albedos are accurate at the one standard deviation level to 0.035 or 7%, a value that is identical to the original standard error of the estimate for the regression formula derived from the NOAA-9 AVHRR and ERBE data. Similarly, the average LW flux difference statistics given at the bottom of Table 2 suggest that the mean AVHRR LW fluxes are accurate to $-1.9 \pm 0.5 \text{ Wm}^{-2}$. The one- σ instantaneous errors are 2.7 Wm^{-2} , a value less than the original regression error. Certainly, the bias in the mean is within the error of the theoretical calculations and the instrument calibrations. If the relative humidity adjusted model TOA fluxes from the SHEBA site are considered as the truth set for the surface data, then the mean bias is only -0.3 Wm^{-2} .

The mean CRF estimates are the differences between the clear sky and total scene radiative fluxes. Thus, a bias error in the fluxes, unless it was scene dependent, would have no effect on the differences. A scene-dependent bias is not evident in the available corroborative data. The random error in both the LW and SW fluxes is reduced to nearly zero for monthly domain means. Thus, uncertainties in the CRF values are primarily dependent on the accuracy of the mean cloud amounts. *Minnis et al.* [2000] estimated that the mean domain cloud fractions are accurate to ± 0.03 compared to surface reports of cloudiness. This translates to a relative error of 4% for the mean cloud amounts listed by *Minnis et al.* [2000]. The uncertainty in CRF due to cloud amount errors is the product either of the uncertainty in cloud fraction and the unit CRF or of the relative cloud fraction uncertainty and the observed CRF. (The unit CRF is simply the CRF divided by the mean cloud fraction.) Thus, from Table 1, the uncertainties in CRFNET are 0.6, 1.0, and 1.3 Wm^{-2} for May, June, and July respectively, at the 1-sigma level. The uncertainties in CRFLW and CRFSW can also be estimated by multiplying them by 0.04.

4.4. Climatology

The mean TOA radiative quantities for the FIRE ACE domain were computed using the ERBE-derived values for the period 1985-1988 for the area encompassed by $72.5^\circ - 80.0^\circ\text{N}$ and $150^\circ - 180^\circ\text{W}$. Table 2 summarizes the ERBE results for each month. These results were derived from NOAA-9 and NOAA-10 data which had complementary errors in their LW fluxes. Thus, the NOAA-10 LW fluxes were too high by $\sim 8 \text{ Wm}^{-2}$, while the NOAA-9 LW fluxes were too low by roughly the same amount. These opposing biases should cancel each other resulting in unbiased mean values because each satellite took 2 years of data. However, the ranges of the mean LW fluxes are probably too large. The values derived during FIRE ACE are within the ERBE ranges for June and July. The mean May albedo during FIRE ACE is 0.02 higher than the previously observed maximum albedo for the month, while the LW flux is the same as the previous maximum. This correction would indicate that the polar snow-cloud system during May 1998 was colder and brighter than normal. Similarly, the net fluxes for the period are within the ERBE ranges except for May. The LW correction would not change that comparison. Thus, except for May, the TOA radiation fields during FIRE ACE were not extraordinary relative to the limited climatology. Although the analysis presented here detected some clear scenes for the regressions shown in Figures 2 and 3, clear-sky data were not available for ERBE because of scene identification problems in domains dominated by snow and ice.

It is difficult to compare the present values to previous results because of the limited domain used here. Earlier estimates are computed for a particular latitude or for nearly the entire

Arctic Ocean. Missing clear-sky data precludes a direct comparison with the ERBE data. The LWCRF values in Table 1 are similar to the results of *Curry and Ebert* [1992] for 80°N, but are 5-10 Wm⁻² less than computed by *Schweiger and Key* [1994] for all ocean areas north of 62.5°N. The SWCRF values are also about half of those calculated by *Schweiger and Key* [1994] for all 3 months and by *Curry and Ebert* [1992] for June and July. During May, the FIRE ACE SWCRF agrees with the latter results. The comparisons are virtually the same for the NETCRF. *Rossow and Zhang* [1995] obtained NETCRF values very close to the current results at 80°N latitude using ISCCP C2 data as reported by *Curry et al.* [1996]. The reasons for the agreement are not clear because the ISCCP C2 cloud amounts are considerably less than those obtained from the FIRE ACE data. Differences in the *Rossow and Zhang* [1995] LWCRF and SWCRF values may be canceling each other resulting in mean NETCRF fluxes that are close to the current results. The *Rossow and Zhang* [1995] data would need to be explored in more detail to resolve the apparent discrepancy between cloud amount and NETCRF. Nevertheless, the current results show that for this spring-to-summer period, the clouds in this domain cause a reduction in the amount radiative energy available to the Earth-atmosphere system. Conclusions about the surface radiative forcing will require analyses of the data taken at the SHEBA site.

4.5. Diurnal variability

The diurnal cycles observed in the hourly means are not particularly strong but appear to be significant with a peak in LW flux near local noon. To better understand these data, the SHEBA Eppley data were examined for a diurnal variation in the surface upwelling flux. Figure 16 shows M_{lw} and M_{lws} for the SHEBA site during May 23-25, 1998, where the subscript S refers to the surface. The average diurnal range in M_{lws} is ~ 35 Wm⁻² while the corresponding M_{lw} range is only 15 Wm⁻². The latter value may be reduced by the lack of samples near the time of the minimum. However, it appears that the M_{lw} is not changing as rapidly as the M_{lws} early in the morning. Thus, 15 Wm⁻² may be a realistic estimate for the diurnal range in M_{lw} . These two daily realizations of the diurnal cycle are much greater than expected from the monthly hourly means. This suggests that the interpolation process for deriving the monthly means may artificially reduce the diurnal amplitude of M_{lw} for clear skies. However, it has minimal effect on the monthly clear-sky LW flux and LWCRF. A straight average of the M_{lw} for all observed clear-sky cases differs by less than 1 Wm⁻² from the interpolated averaging result.

Examination of the few clear-sky days during June and July shows a much reduced diurnal amplitude suggesting that the melt ponds are absorbing the solar radiation with the bulk of the heating going into melting of ice, resulting in a gradual increase in the skin temperature. The lack of a significant diurnal cycle is similar to the response of the ocean to solar absorption. During May, the larger diurnal range suggests that a thin surface layer is warming, because the radiation is not penetrating the surface as much as it does later in the season when ponds are present. The diminished diurnal amplitude of M_{lw} compared to that of M_{lws} is consistent with the relative contribution of the atmosphere to M_{lw} . As shown in earlier calculations, the atmosphere accounts for about 50% of the TOA LW flux. Therefore, the diurnal amplitude in M_{lw} should be roughly half of M_{lws} as seen in Figure 16.

6. CONCLUDING REMARKS

The results presented here show a negative cloud forcing at the TOA during late spring and early summer over the greater SHEBA domain. The small contrast between clear and cloudy scenes found during May for both shortwave and longwave radiation gives way to a more

substantial shortwave forcing during July. The clouds are a dominant feature, covering an average of 70 - 80% of the domain; but because they radiate at nearly the same mean temperature as the surface, they only slightly reduce the loss of longwave radiation to space. The comparable radiating temperatures of the clouds and the surface suggest that much of the surface-emitted radiation is returned by the clouds. Thus, the cloud radiative forcing at the surface may be significantly different than that at the TOA.

A surprising finding of this study relates to the diurnal variation in the surface-emitted longwave radiation. While the snow is frozen, the surface radiation cycle is similar to that over land. Under clear skies, the surface heating varies sinusoidally with a maximum near noon. Without a sunset, however, the surface does not experience the exponential cooling observed at lower latitudes over land. As the summer progresses, the Arctic surface behaves more like the ocean in that a small diurnal signal occurs, but its phase is more difficult to discern because of a relatively large noise in the small signal. This change in the diurnal cycle from more land-like to more ocean-like behavior suggests that a different approach is needed for modeling the diurnal variation of clear-sky longwave flux for snow-covered surfaces for radiation budget monitoring. Current approaches assume a linear variation like that used over ocean. A more sinusoidal interpolation may be required to improve the accuracy of the satellite-derived radiation budgets in polar regions.

A complete, accurate radiative depiction of the Arctic atmosphere is closer to realization than before FIRE ACE because of the excellent agreement found between the satellite and model-adjusted fluxes. The accuracy of the AVHRR-derived fluxes is within the expected uncertainties for both the satellite-model and ERBE regression datasets. Thus, they can be used reliably with the surface datasets. Using SHEBA radar data to define the locations of the clouds, together with refined application of the satellite data to determine the cloud optical properties and the surface radiometer measurements to determine the surface fluxes, will enable the development of a three-dimensional radiation profile of the troposphere within the SHEBA domain. In situ FIRE aircraft data, however, will be needed to aid the refinement of techniques for deriving cloud optical depth from satellite data over the Arctic. Methods based on currently available satellite instruments tend to overestimate cloud optical depth due to the sensitivity of the retrievals in bright background, low contrast scenes [e.g., *Dong et al.* 2000]. Due to this uncertainty, cloud optical depths were not derived for this study. Additional analyses are needed to provide a comprehensive and reliable cloud optical depth dataset for this period.

This study has clearly demonstrated the capabilities for determining cloud and clear radiative fluxes over the Arctic during summer using carefully analyzed AVHRR with a regionally dependent narrowband-to-broadband regression formula. With the development of similar regression formulae for other seasons, it should be possible to provide detailed flux data over the Arctic for the entire SHEBA period using the AVHRR data. With the year-long SHEBA surface dataset, it should then be possible to accurately constrain the energy budget of the Arctic Ocean at the surface and at the top of the atmosphere for an entire annual cycle.

Acknowledgments.

Special thanks to Bill Smith, Jr., Mandy Khaiyer, Pat Heck, Kirk Ayers, Shalini Mayor, and Anthony Bucholtz for monitoring and collecting the data during FIRE ACE. This research was supported by the NASA Earth Sciences Enterprise Radiation Sciences Program FIRE Project and by the Environmental Sciences Division of the U.S. Department of Energy Interagency Agreement DE-AI02-97ER62341 as part of the Atmospheric Radiation Measurement (ARM) Program sponsored by the Office of Science, Office of Biological and Environmental Research, Environmental Sciences Division. The ship data were also obtained from the ARM Program and from the NSF-SHEBA program under agreement #OPP-9701730. We thank our colleagues in the SHEBA Atmospheric Surface Flux Group, Ed Andreas, Chris Fairall, Peter Guest, and Ola Persson, for help collecting and processing the data. The National Science Foundation supported the processing with grants to the U.S. Army Cold Regions Research and Engineering Laboratory, NOAA's Environmental Technology Laboratory, and the Naval Postgraduate School.

References

- Andreas, Edgar L, C. W. Fairall, P. S. Guest, and P. Ola G. Persson, An overview of the SHEBA atmospheric surface flux program. *Proc. 5th Conf. On Polar Meteorology and Oceanography*, Jan. 10-15, Dallas TX, Amer. Meteor. Soc., 411-416, 1999.
- Bannehr, L. and V. Glover, Preprocessing of airborne pyranometer data. NCAR Technical Note *NCAR/TN-364+STR*, National Center for Atmospheric Research, Boulder, CO, 1991.
- Barkstrom, B. R., E. Harrison, G. Smith, R. Green, J. Kibler, R. Cess, and the ERBE Science Team, Earth Radiation Budget Experiment (ERBE) archival and April 1985 results, *Bull. Am. Meteorol. Soc.*, **70**, 1254-1262, 1989.
- Bowker, D.E., R.E. Davis, D.L. Myrick, K. Stacy, and W.T. Jones, Spectral reflectances of natural targets for use in remote sensing studies, *NASA Ref. Pub. 1139*, June 1985.
- Charlock, T. P. and T. L. Alberta, The CERES/ARM/GEWEX Experiment (CAGEX) for the retrieval of radiative fluxes with satellite data. *Bull. Amer. Meteor. Soc.*, **77**, 2673-2683.
- Curry, J. A. and E. E. Ebert, Annual cycle of radiation fluxes over the Arctic Ocean: Sensitivity to cloud optical properties. *J. Climate*, **5**, 1274-1280, 1992.
- Curry, J. A., W. B. Rossow, D. Randall, and J. L. Schramm, Overview of Arctic cloud and radiation characteristics. *J. Climate*, **9**, 1731-1764, 1996.
- Curry, J. A., P. Hobbs, M. D. King, D. Randall, P. Minnis, T. Uttal, G. A. Isaac, J. Pinto, et al. FIRE Arctic Clouds Experiment. *Bull. Am. Meteorol. Soc.*, **81**, 5-29, 2000.
- d'Almeida, G. A., P. Koepke, and E. P. Shettle, Atmospheric aerosols - global climatology and radiative characteristics. A. Deepak Publishing, Hampton, Virginia, 561 pp., 1991.
- Doelling, D. R., L. Nguyen, W. L. Smith, Jr., and P. Minnis, Comparison of ARM GOES-derived broadband fluxes and albedos with broadband data from ARM-UAV, ScaRaB, and CERES. *Proc. 8th Ann. ARM Sci. Team Mtg.*, Tuscon, AZ, March 23-27, 201-205, 1998.
- Dong, X., G.G. Mace, P. Minnis, and D.F. Young, Arctic stratus cloud their effect on the surface radiation budget; Selected cases from FIRE ACE. Submitted to *J. Geophys. Res.*, this issue, 2000.
- Fu, Q. and K. N. Liou, Parameterization of the radiative properties of cirrus clouds. *J. Atmos. Sci.* **50**, 2008-2025, 1993.

- Green, R. N. and L. M. Avis, Validation of ERBS scanner radiances. *J. Atmos. Ocean. Technol.*, **13**, 851-862, 1996.
- Grenfell, T. C., S. G. Warren, and P. C. Mullen, Reflection of solar radiation by the Antarctic snow surface at ultraviolet, visible, and near-infrared wavelengths, *J. Geophys. Res.*, **99**, 18669-18684, 1994.
- Gupta, S. K., A. C. Wilber, N. A. Ritchey, W. L. Darnell, F. G. Rose, and T. P. Charlock, Regrid Humidity and Temperature Fields (Subsystem 12.0) Clouds and the Earth's Radiant Energy System (CERES) algorithm theoretical basis document, Volume IV: Determination of surface and atmosphere fluxes and temporally and spatially averaged products (Subsystems 5-12)", *NASA RP 1376 Vol. 4*, pp. 163-172, 1995.
- Harrison, E. F., P. Minnis, B. R. Barkstrom, V. Ramanathan, R. D. Cess, and G. G. Gibson, Seasonal variation of cloud radiative forcing derived from the Earth Radiation Budget experiment. *J. Geophys. Res.*, **95**, 18,687-18,703, 1990.
- Haywood, J. M., V. Ramaswamy, and B. J. Soden, Tropospheric aerosol climate forcing in clear-sky satellite observations over the oceans, *Science*, **283**, 1299-1303.
- Hess, M., P. Koepke, and I. Schult, Optical properties of aerosols and clouds: The software package OPAC. *Bull. Amer. Meteor. Soc.*, **79**, 831-844, 1998.
- Kato, S., T. P. Ackerman, E. E. Clothiaux, J. H. Mather, G. G. Mace, M. L. Wesely, F. Murcray, and J. Michalsky, Uncertainties in modeled and measured clear-sky surface shortwave irradiances. *J. Geophys. Res.*, **102**, 25, 881-25,898, 1997.
- Key, J. and A.J. Schweiger, Tools for atmospheric radiative transfer: Streamer and Fluxnet. *Computers and Geosciences*, **24**, 443-451, 1998.
- Minnis, P., Doelling, C. Venkatesan, D. A. Spangenberg, L. Nguyen, R. Palikonda, T. Uttal, M. Shupe, and R. F. Arduini, Arctic cloud coverage during FIRE ACE derived from AVHRR data. *J. Geophys. Res.*, this issue, 2000.
- Minnis P. and E. F. Harrison, Diurnal variability of regional cloud and clear-sky radiative parameters derived from GOES data; Part I: Analysis method. *J Climate Appl. Meteorol.*, **23**, 993-1011, 1984.
- Minnis P., P. W. Heck, and D. F. Young, Inference of cirrus cloud properties using satellite-observed visible and infrared radiances. Part II: Verification of theoretical cirrus radiative properties. *J. Atmos. Sci.*, **50**, 1305-1322, 1993.
- Minnis, P. and W. L. Smith, Jr., Cloud and radiative fields derived from GOES-8 during SUCCESS and the ARM-UAV Spring 1996 Flight Series. *Geophys. Res. Ltrs.*, **25**, 1113-1116, 1998.
- Minnis, P., D. F. Young, and E. F. Harrison, Examination of the relationship between infrared window radiance and the total outgoing longwave flux using satellite data. *J. Climate*, **4**, 1114-1133, 1991.
- Perovich, D. K., E. L. Andreas, J. A. Curry, H. Elken, C. W. Fairall, T. C. Grenfell, P. S. Guest, J. Intrieri, et al., Year on ice gives climate insights. *Eos*, **80**, 481-486, 1999.
- Ramanathan, V., R. D. Cess, E. F. Harrison, P. Minnis, B. R. Barkstrom, E. Ahmad, and D. Hartmann, Cloud-radiative forcing and climate: Results from the Earth Radiation Budget Experiment. *Science*, **243**, 57-63, 1989.
- Rossow, W. B. and R. A. Schiffer, Advances in understanding clouds from ISCCP. *Bull. Am. Meteorol. Soc.*, **80**, 2261-2287, 1999.

- Rossow, W. B. and Y.-C. Zhang, Calculation of surface Rossow, W. B. and and top-of-atmosphere radiative fluxes from physical quantities based on ISCCP datasets. Part II: Validation and first results. *J. Geophys. Res.*, **100**, 1167-1197, 1995.
- Schweiger, A. J. and J. R. Key, Arctic Ocean radiative fluxes and cloud forcing estimated from the ISCCP C2 cloud dataset, 1983-1990. *J. appl. Meteor.*, **33**, 948-963, 1994.
- Spinhirne, J. D., Visible and near IR lidar backscatter observations on the GLOBE Pacific survey missions. *Proc. AMS 7th Symp. on Meteorol. Observations and Instrumentation*, New Orleans, LA, J261-J264.
- Stokes, G. M. and S. E. Schwartz, The Atmospheric Radiation Measurement (ARM) Program: Programmatic background and design of the Cloud and Radiation Testbed. *Bull. Am. Meteorol. Soc.*, **75**, 1201-1221, 1994.
- Suttles, J. T., R. N. Green, P. Minnis, G. L. Smith, W. F. Staylor, B. A. Wielicki, I. J. Walker, D. F. Young, V. R. Taylor, and L. L. Stowe, Angular radiation models for Earth-atmosphere system: Volume I - Shortwave radiation. *NASA RP 1184*, 144 pp., 1988.
- Thomas, D., J. P. Duvel, and R. Kandel, Diurnal bias in calibration of broad-band radiance measurements from space. *IEEE Trans. Geosci. And Remote Sens.*, **33**, 670-683, 1995.
- Valero, F. P. J., R. D. Cess, M. Zhang, S. K. Pope, A. Bucholtz, B. C. Bush, and J. Vitko, Jr., Absorption of solar radiation by clouds: Interpretations of colocated measurements. *J. Geophys. Res.*, **102**, 29,917-29,927, 1997.
- Valero, F. P. J., P. Minnis, S. K. Pope, A. Bucholtz, B. C. Bush, D. R. Doelling, W. L. Smith, Jr., and X. Dong, The absorption of solar radiation by the atmosphere as determined using consistent satellite, aircraft, and surface data during the ARM Enhanced Short-Wave Experiment (ARESE). In press, *J. Geophys. Res.*, October, 1999.
- Wielicki, B. A., R. D. Cess, M. D. King, D. A. Randall, and E. F. Harrison, Mission to Planet earth: Role of clouds and radiation in climate. *Bull. Amer. Meteor. Soc.*, **76**, 2125-2153, 1995.
- Young, D. Y., P. Minnis, D. R. Doelling, G. G. Gibson and T. Wong, Temporal interpolation methods for the Clouds and the Earth's Radiant Energy System (CERES) Experiment. *Jour. Appl. Meteor.* **37**, 572-590, 1998.

FIGURE CAPTIONS

Figure 1. Example of the model computations of SW albedo profiles used to correct the aircraft albedos to the TOA.

Figure 2. Scatterplot and regression fits for matched NOAA-9 AVHRR VIS and ERBE SW albedos for May-July 1986 for 2.5° regions between 65 and 75°N and 135 and 170°W .

Figure 3. Same as figure 2 except for matched IR and LW fluxes.

Figure 4. NOAA-12 AVHRR visible image and scene identification, albedo, and LW flux maps at 1936 UTC, 19 May 1998 over the Arctic Ocean. SHEBA camp denoted by “S.”

Figure 5. Distribution of clear and total SW albedo for FIRE ACE during May, June, and July 1998. Mean position of SHEBA camp denoted by the small box.

Figure 6. Same as Figure 5, except for clear and total LW flux.

Figure 7. Same as Figure 5, except for mean SW, LW, and net CRF.

Figure 8. Diurnal variation of mean clear and total SW albedos during FIRE ACE. Also shown is the variation of μ_0 during July.

Figure 9. Diurnal variation of mean clear and total LW fluxes during FIRE ACE.

Figure 10. Diurnal variation of mean CRF during FIRE ACE.

Figure 11. Comparison of clear-sky TOA albedos from model calculations using SHEBA tower surface albedos and from coincident AVHRR data during FIRE ACE. Line of agreement is shown for reference.

Figure 12. Comparison of TOA clear-sky LW fluxes using SHEBA tower upwelling LW fluxes in the models. Line of agreement is shown for reference.

Figure 13. Comparison of downwelling LW flux at the SHEBA site computed from FL model using radiosonde profiles and measured by uplooking Eppley pyregeometers during FIRE ACE. Line of agreement is shown for reference.

Figure 14. Comparison of TOA albedos derived from AVHRR and from C-130 Eppley pyranometers and the RAMS TSBR radiometers during May and July 1998. Line of agreement is shown for reference.

Figure 15. Comparison of TOA LW fluxes derived from AVHRR and C-130 Eppley pyregeometers during July 1998. Solid line is the line of agreement.

Figure 16. Diurnal variation of surface and TOA fluxes at the SHEBA camp for clear days May 23-25, 1998.

Table 1. Mean radiation quantities from AVHRR for FIRE ACE for 72.5 - 80.0°N and 150 - 180°W.

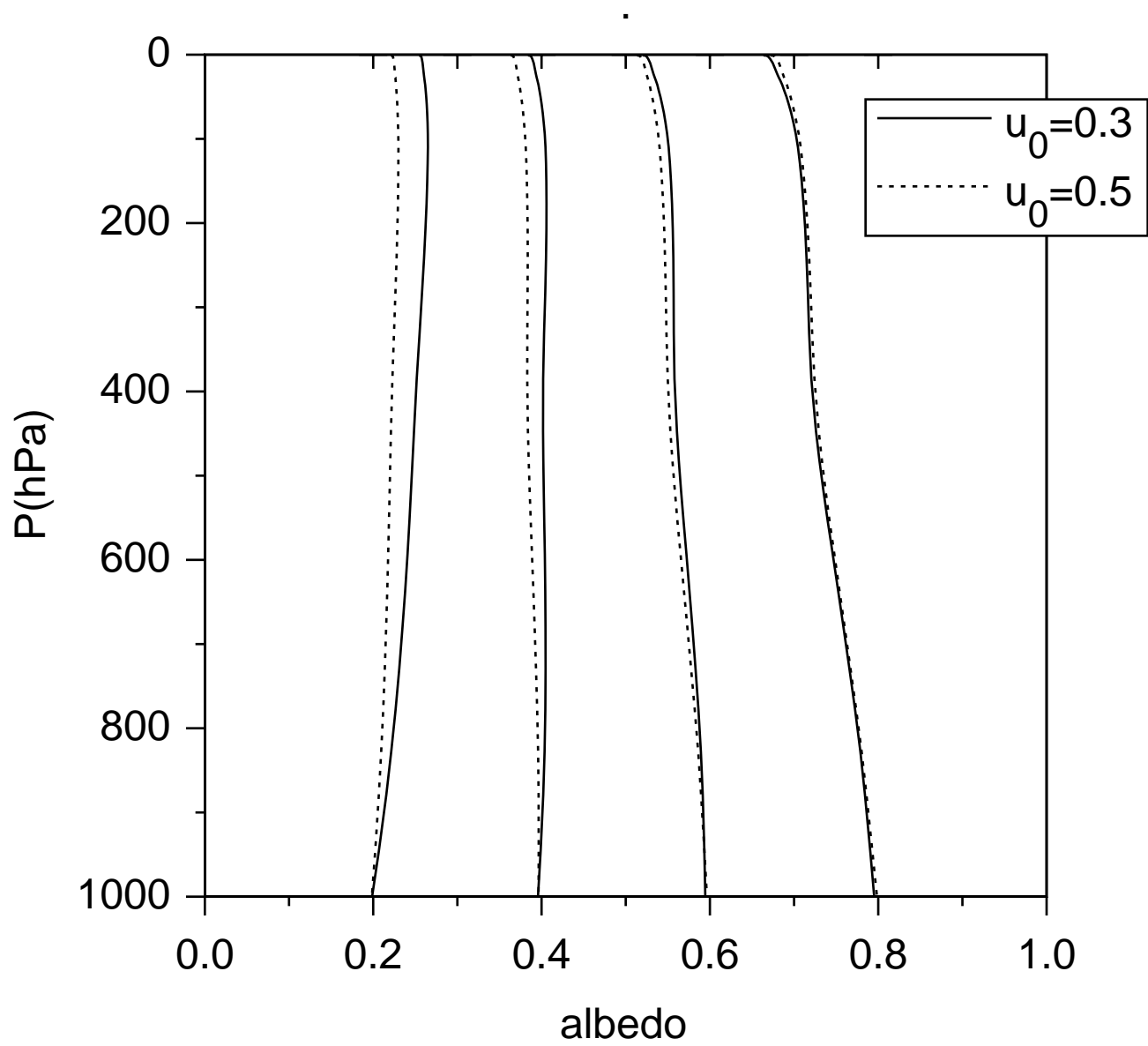
Property	<u>May</u>			<u>June</u>			<u>July</u>		
	total	clear	CRF	total	clear	CRF	total	clear	CRF
α_{SW}	0.695	0.642		0.592	0.524		0.510	0.424	
M_{SW}, Wm^{-2}	291.8	269.7	-22.1	298.4	264.1	-34.3	235.6	196.1	-39.5
M_{LW}, Wm^{-2}	217.4	224.5	7.1	225.2	234.6	9.4	228.4	237.2	8.8
M_{NET}, Wm^{-2}	-89.2	-74.3	-14.9	-19.9	5.0	-24.9	-2.1	28.7	-30.7

Table 2. Summary of TOA albedo and LW flux comparisons using aircraft and surface radiometer data.

Data & models	$\alpha_{\text{sw}}(\text{AVHRR}) - \alpha_{\text{sw}}(\text{model})$			$M_{\text{lw}}(\text{AVHRR}) - M_{\text{lw}}(\text{model}), \text{Wm}^{-2}$		
	mean	σ	n	mean	σ	n
Surface						
FL	-0.001	0.035	13	-4.2	2.1	13
Streamer	-0.012	0.023	13	-2.5	3.5	13
average	-0.007	0.029	13	-3.3	2.8	13
FL, adjust	-	-	-	-0.3	2.5	13
C-130Q, FL						
Eppley	0.023	0.029	15	-0.2	2.6	10
RAMS	-0.004	0.029	16	-	-	-
average	0.009	0.029	16			
Average, sfc + aircraft	0.001	0.029	29	-1.9	2.7	23

Table 3. Mean radiative properties from ERBE for 1985-1988 for 72.5 - 80.0°N and 150 - 180°W.

	May		June		July	
	mean	range	mean	range	mean	range
α_{SW}	0.66	0.64 - 0.68	0.60	0.57 - 0.62	0.53	0.50 - 0.56
M_{LW} , Wm^{-2}	207.5	203 - 212	224.4	219 - 228	227.1	221 - 231
M_{NET} , Wm^{-2}	-67.6	-59 - -74	-24.9	-9 - -32	-7.5	+1 - -17



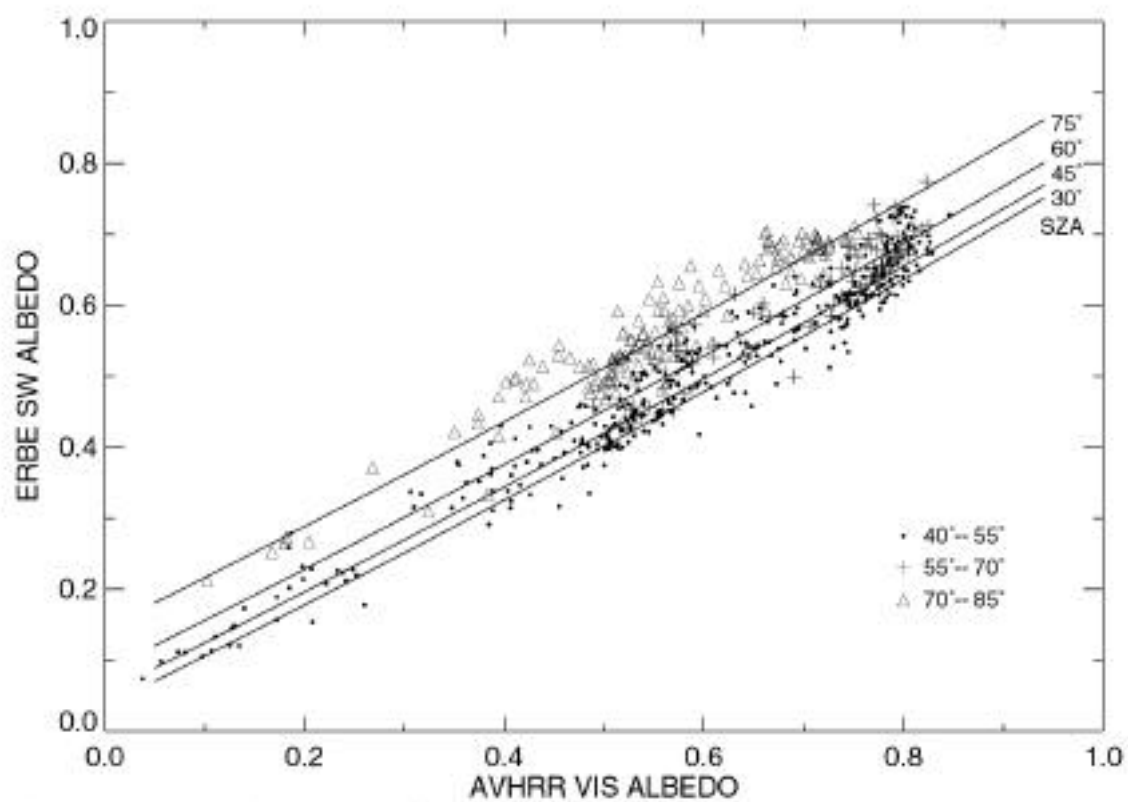


Figure 2. Scatterplot and regression fits for matched NOAA-9 AVHRR VIS and ERBE SW albedos for May-July 1986 for 2.5° regions between 65 and 75°N and 135 and 170°W.

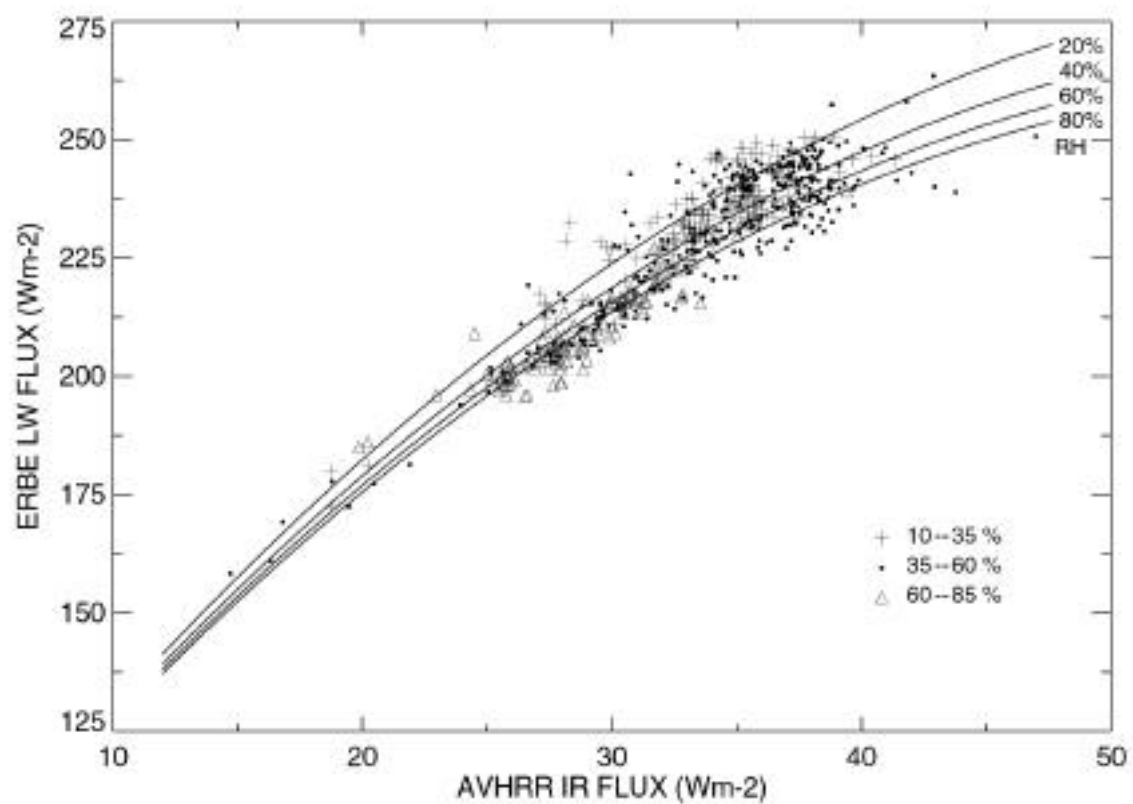
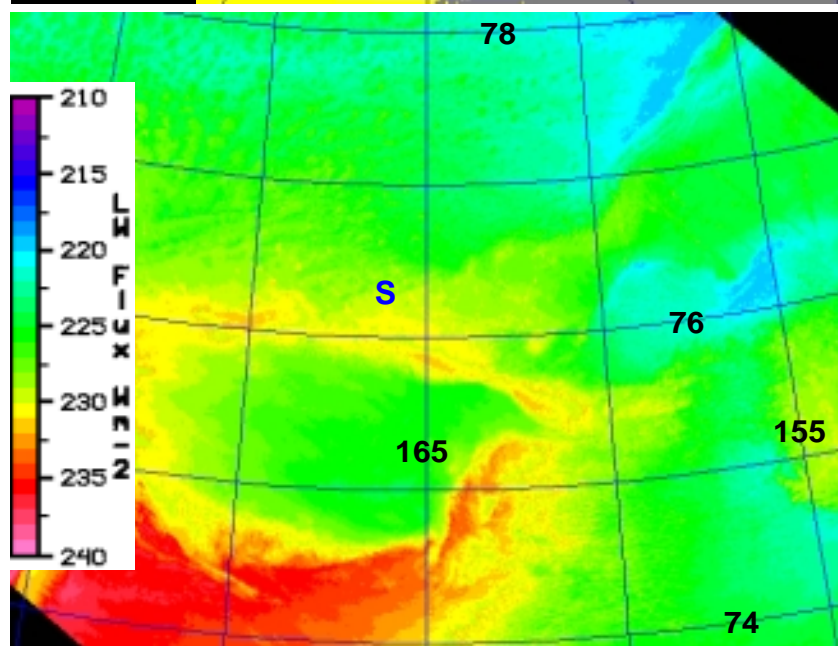
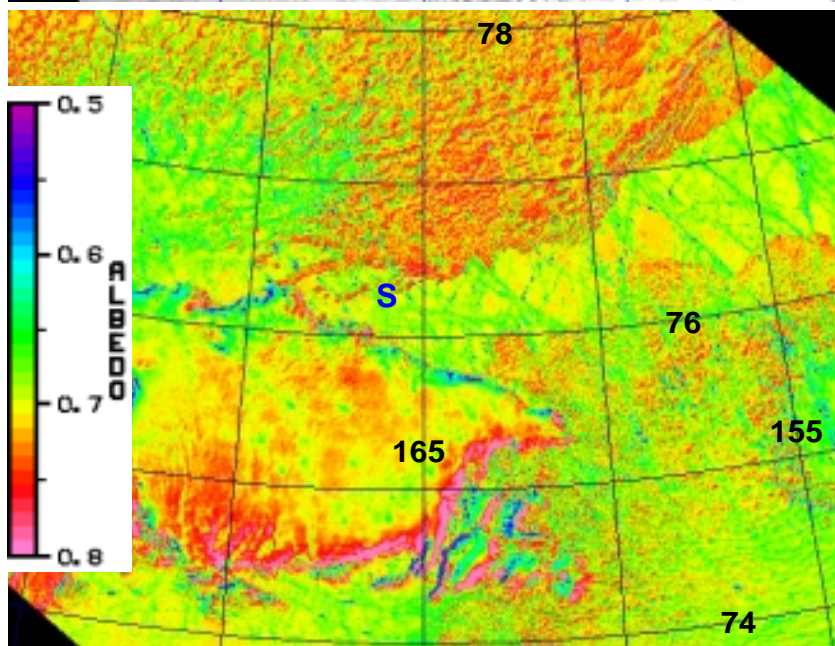
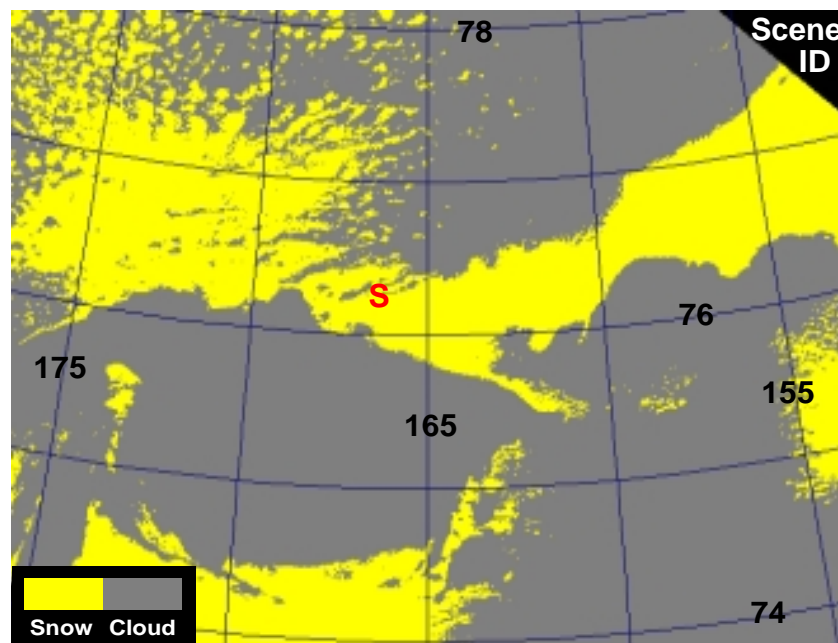
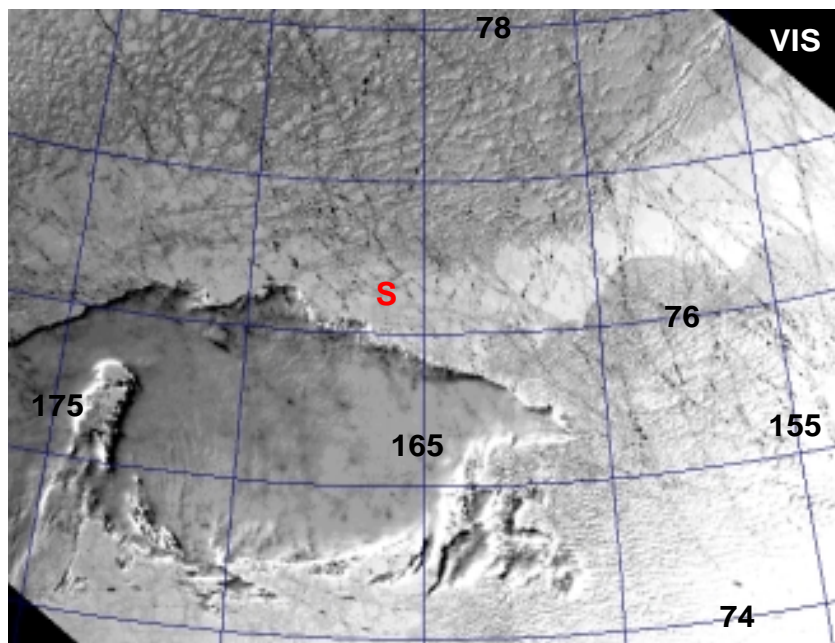
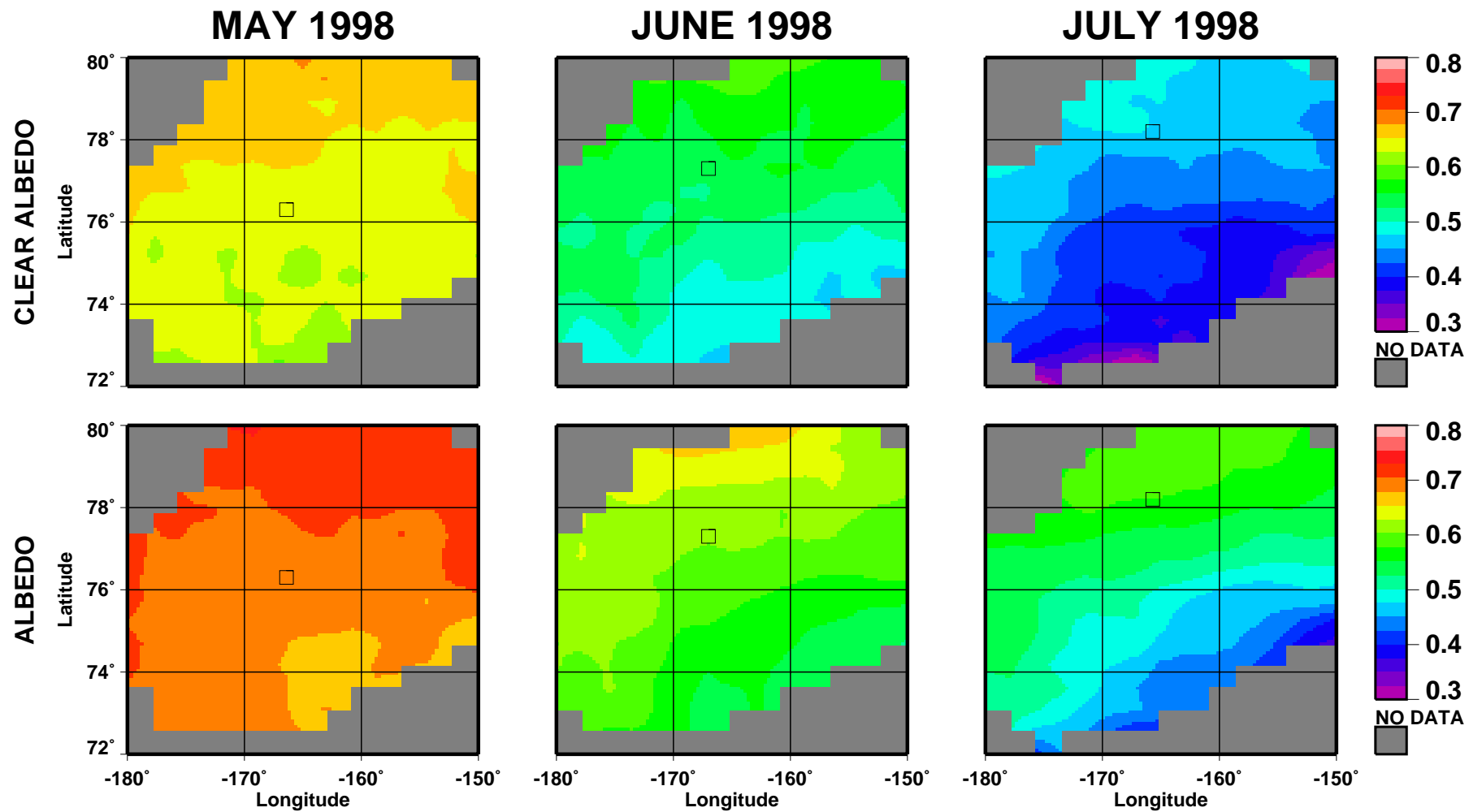
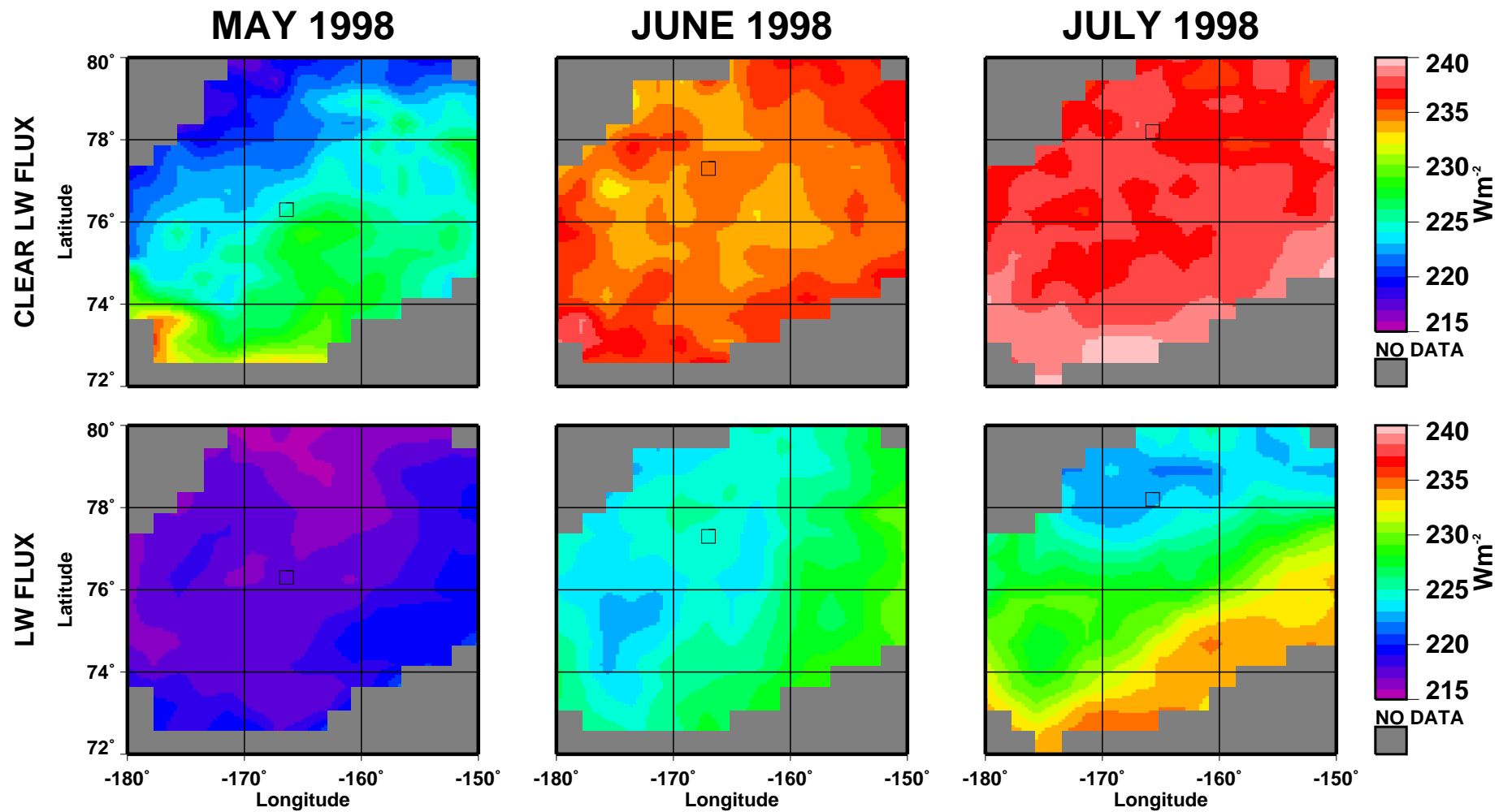
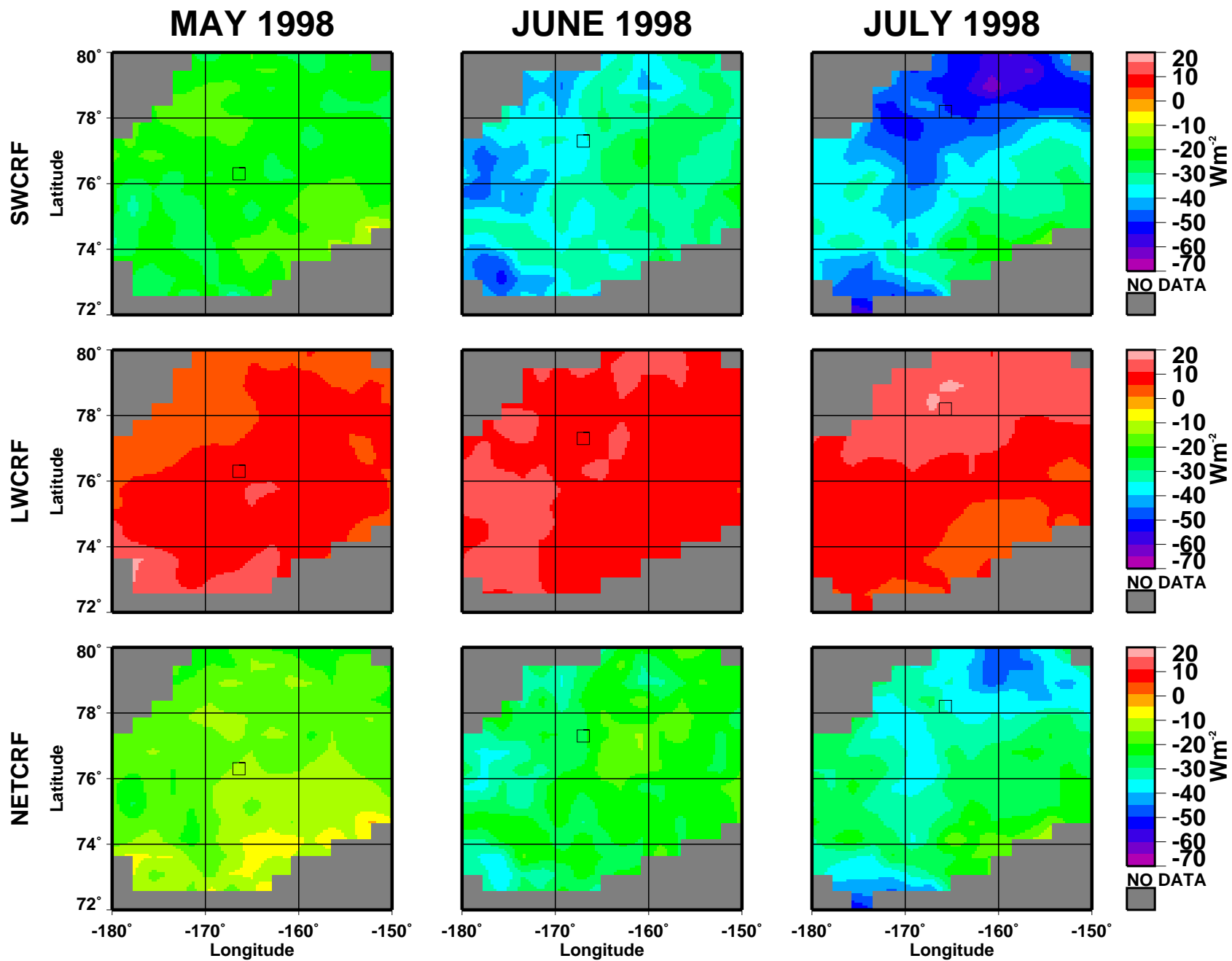


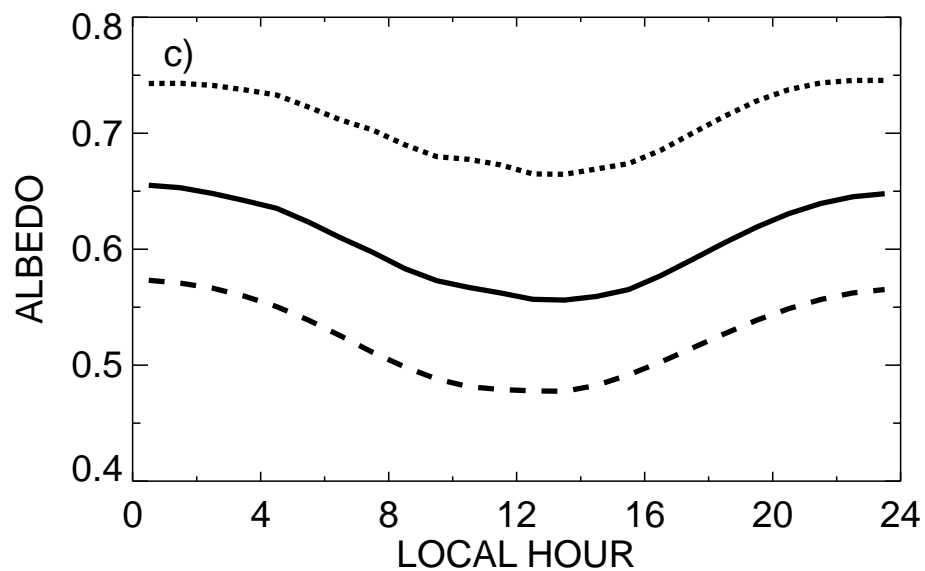
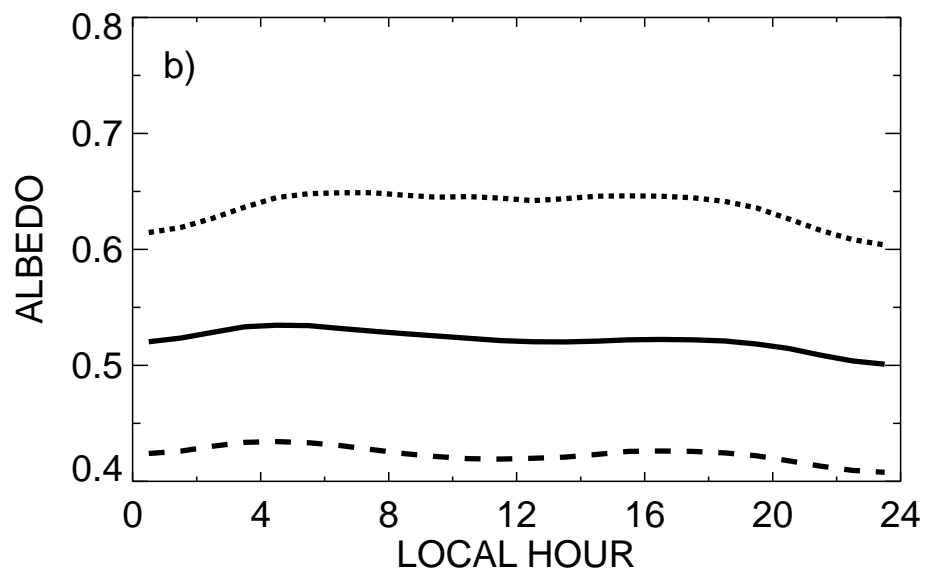
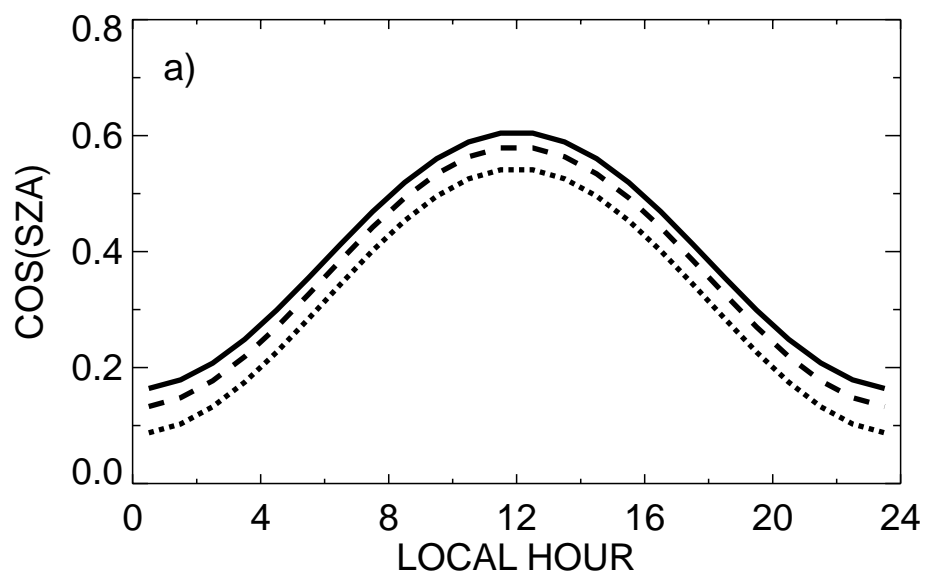
Figure 3. Same as figure 2 except for matched IR and LW fluxes.

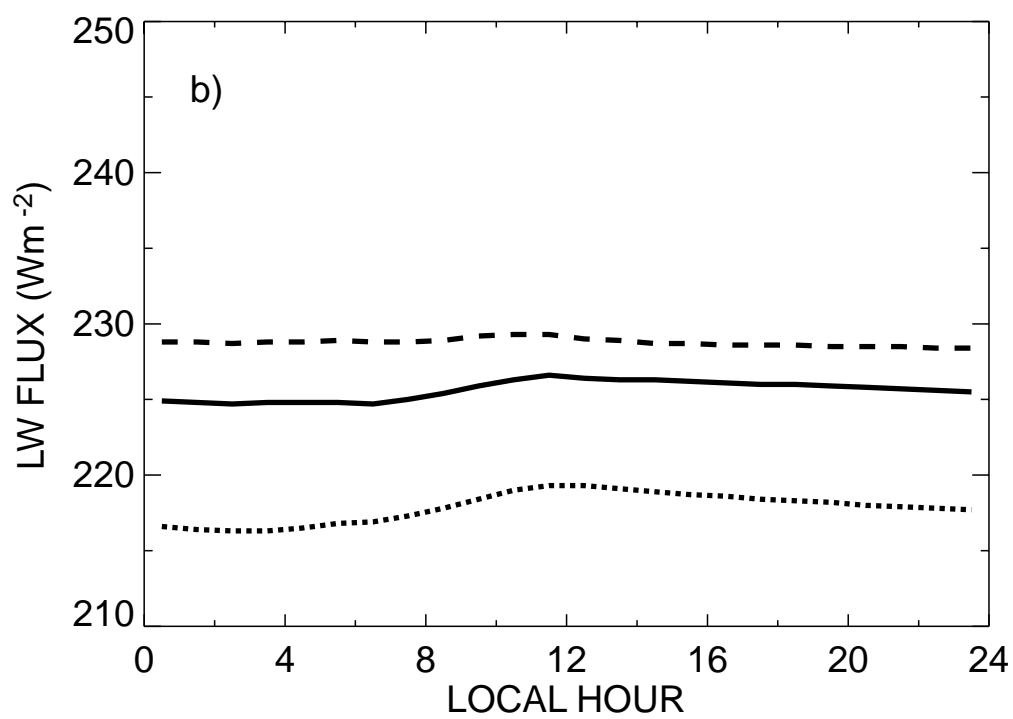
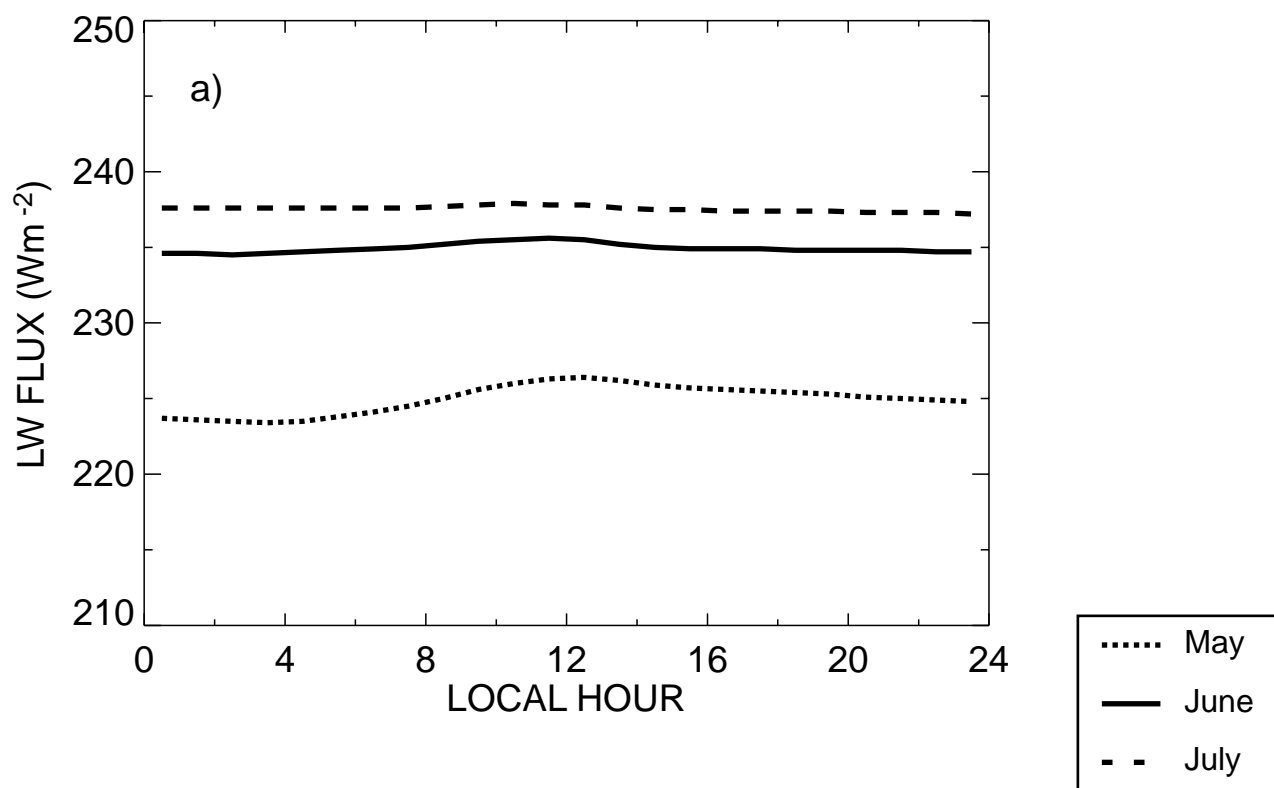


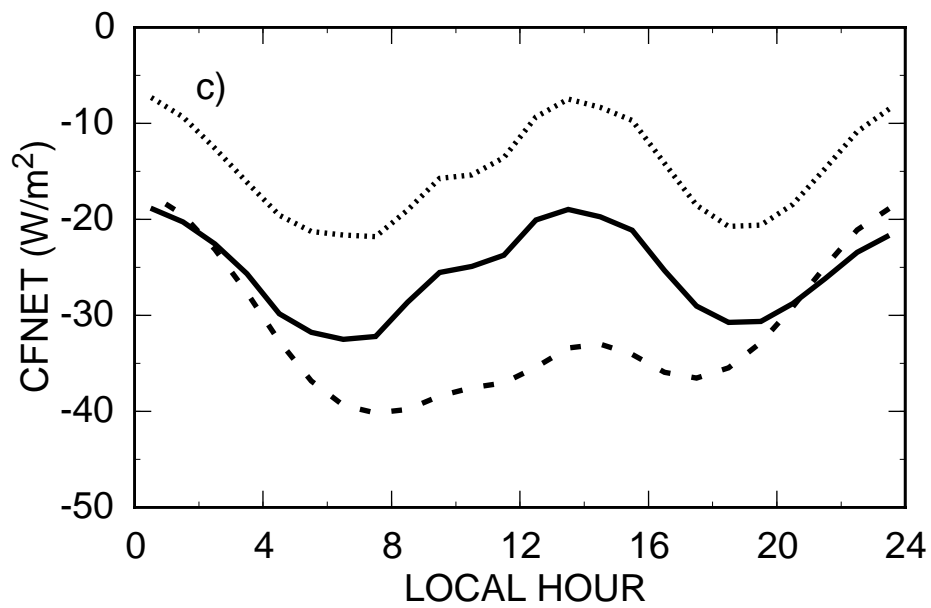
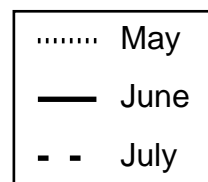
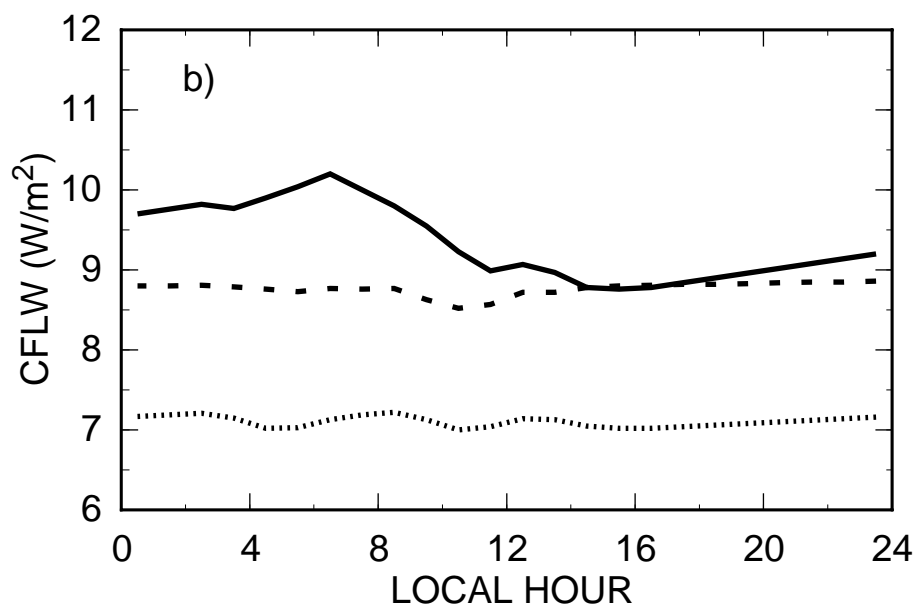
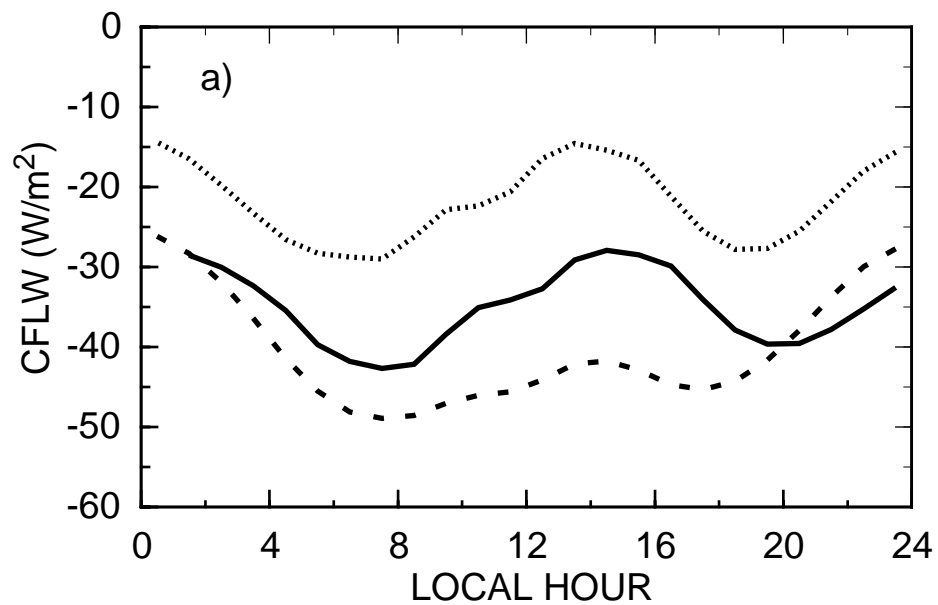












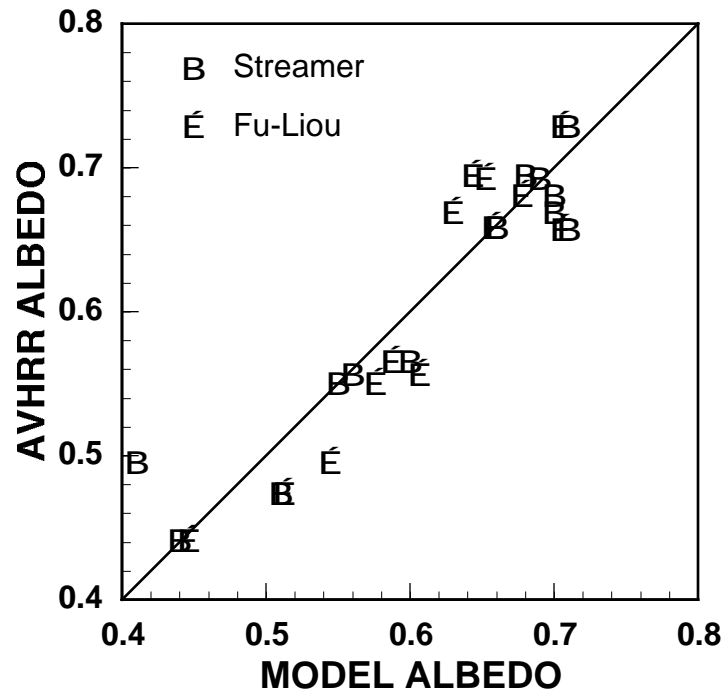


Figure 11. Comparison of clear-sky TOA albedos from model calculations using SHEBA tower surface albedos and from coincident AVHRR data during FIRE ACE. Line of agreement is shown for reference.

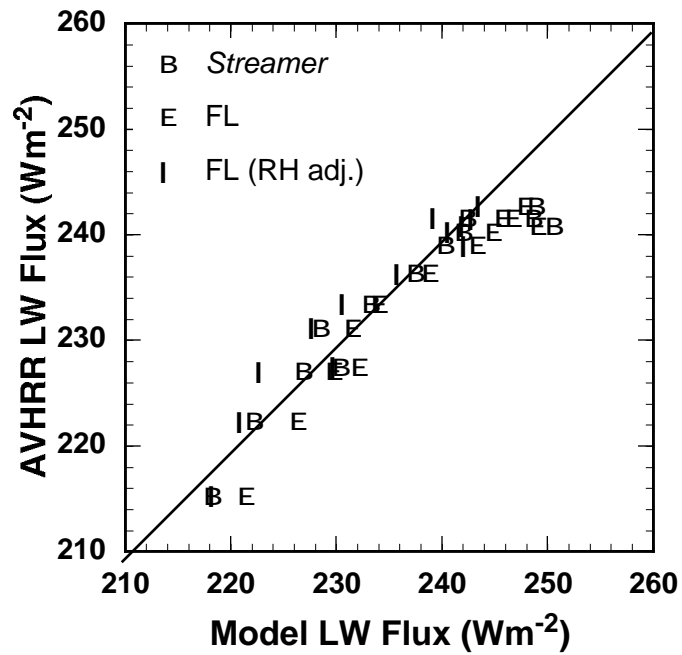


Figure 12. Comparison of TOA clear-sky LW fluxes using SHEBA tower upwelling LW fluxes in the models. Line of agreement is shown for reference.

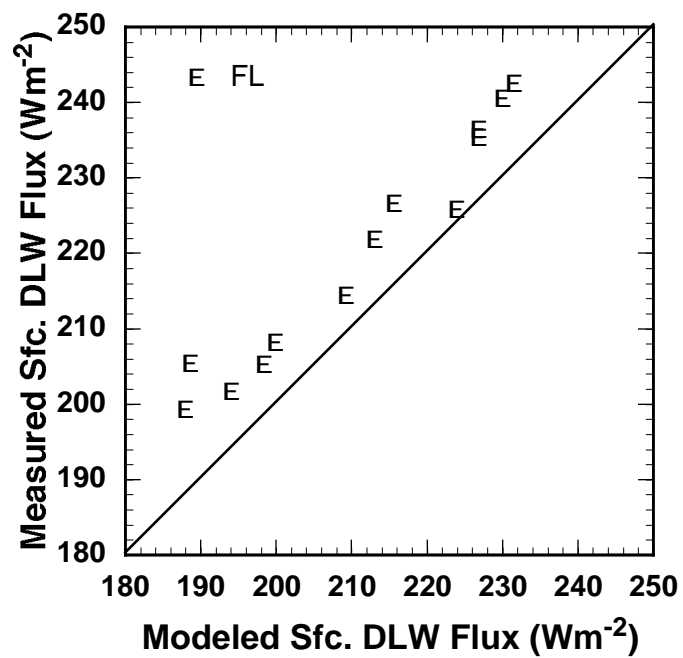


Figure 13. Comparison of downwelling LW flux at the SHEBA site computed from FL model using radiosonde profiles and measured by uplooking Eppley pyregeometers during FIRE ACE. Line of agreement is shown for reference.

